Chinese Chemical Letters 36 (2025) 110006

Contents lists available at ScienceDirect

Chinese Chemical Letters

journal homepage: www.elsevier.com/locate/cclet

Research progress of inorganic sodium ion conductors for solid-state batteries

Qiao Wang[a,1], Ziling Jiang[b,1], Chuang Yu[b,*], Liping Li[a,*], Guangshe Li[a,*]

[a] State Key Laboratory of Inorganic Synthesis and Preparative Chemistry, College of Chemistry, Jilin University, Changchun 130012, China
[b] State Key Laboratory of Advanced Electromagnetic Engineering and Technology, School of Electrical and Electronic Engineering, Huazhong University of Science and Technology, Wuhan 430000, China

ARTICLE INFO

Article history:
Received 8 February 2024
Revised 14 March 2024
Accepted 13 May 2024
Available online 18 May 2024

Keywords:
Inorganic sodium ion conductors
Structure
Modification
All-solid-state sodium-ion batteries
Electrochemical performance

ABSTRACT

For large-scale energy storage devices, all-solid-state sodium-ion batteries (SIBs) have been revered for the abundant resources, low cost, safety performance and a wide operating temperature range. Na-ion solid-state electrolytes (Na-ion SSEs) are the critical parts and mostly determine the electrochemical performance of SIBs. Among the studied ones, inorganic Na-ion SSEs stand out for their good safety performance and high ionic conductivity. In this review, we outline the research progress of inorganic SSEs in SIBs based on the perspectives of crystal structure, performance optimization, synthesis methods, all-solid-state SIBs, interface modification and related characterization techniques. We hope to provide some ideas for the design of future high-performance Na-ion SSEs.

1. Introduction

Na-ion batteries (SIBs) are regarded as a promising next generation electrochemical energy storage technology due to the abundance, wide distribution, low cost of sodium resources, as well as similar chemical properties of Na and Li elements, which have been widely investigated in the past decades [1–10]. Kummer *et al.* first reported a fast Na-ion conduction in Na-β''-Al_2O_3 in 1967 [11]. Later, Ford *et al.* designed a high-temperature Na-S battery based on this material in 1968. Since then, researchers have made a lot of efforts in sodium ion battery. Up to data, more than 20 companies around the world are working on the development of SIBs, and SIBs are gradually achieving practical application. Traditional SIBs using liquid organic electrolytes are prone to volatility and leakage, resulting in safety risks [12–14]. Differently, all-solid-state SIBs are significantly safer because of the use of solid-state electrolytes (SSEs) with non-volatile and non-leakage features [15–18]. More importantly, solid-state SIBs with sodium metal as anode can provide high energy density comparing to hard carbon anode.

Solid-state SIBs have become one of hot topics in the future energy storage field [19,20]. The ionic conductivity and stability of SSEs as well as their compatibility with electrode materials in solid-state SIBs are the important factors affecting the performance of SIBs [21–23]. Therefore, it is imperative to synthesize and optimize new Na-ion SSE materials in addition to optimizing and improving electrode materials. Na-ion SSEs can be mainly divided into two catalogs: inorganic and organic polymer SSEs. Although organic polymer SSEs have good flexibility and low interfacial resistance with electrodes [24–29], they face some intrinsic natures, such low ionic conductivity at r.t., narrow electrochemical window, and poor mechanical strength, which hinders their application [30–32]. Adding inorganic fillers and synthesizing inorganic-organic polymer composites are two widely adopted strategies to improve ionic conductivity of organic polymer SSEs. Compared with polymer SSEs, inorganic ones have higher ionic conductivity at r.t. ($>10^{-3}$ S/cm), wider electrochemical window, better thermal stability, and higher mechanical strength can effectively inhibit the growth of sodium dendrites, and thus have been attracted more attention [23,33–36].

Over the past decades, considerable progress about the Na-ion SSEs have been achieved. As early as 1968, the fast conduction of sodium ions in oxide Na-β''-Al_2O_3 was reported by Kummer *et al.* firstly [11]. After that, the Nasicon material with the general formula $Na_{1+x}Zr_2Si_xP_{3-x}O_{12}$ ($0 \le x \le 3$) was proposed by Goodenough and Hong *et al.* in 1976 [37,38]. The highest ionic conductivity was obtained up to 6.7×10^{-4} S/cm and 0.2 S/cm at 25 °C and 300 °C, respectively, for $Na_3Zr_2Si_2PO_{12}$ (*i.e.*, $x = 2$ of $Na_{1+x}Zr_2Si_xP_{3-x}O_{12}$). In 2011, Evstygneeva *et al.* reported a new type of oxide Na-ion SSE with layered structure [39]. In addition to oxides mentioned above,

* Corresponding authors.
E-mail addresses: cyu2020@hust.edu.cn (C. Yu), lipingli@jlu.edu.cn (L. Li), guangshe@jlu.edu.cn (G. Li).
[1] These authors contributed equally to this work.

https://doi.org/10.1016/j.cclet.2024.110006
1001-8417/

anti-perovskites, complex hydride, and sulfide SSEs are also being studied extensively [40–42]. The highest Na-ion conductivity at r.t. is reached as high as 7×10^{-2} S/cm for $Na_2(CB_9H_{10})(CB_{11}H_{12})$. A systematic understanding of the structure, synthesis, modification, and application of Na-ion SSEs is very important, but urgent for the development of all-solid-state SIBs with high performance.

In this review, we focus on inorganic Na-ion SSEs, including Na-β/β''-Al_2O_3, Nasicon, layered oxides, anti-perovskite, complex hydrides and halides, *etc.* We first discuss the mechanism of Na-ion transport and the structures of these typical SSEs. We then specify the synthesis methods and enumerate the strategies for enhancing the conductivity and stability of Na-ion SSEs. After summarizing the application of SSEs in solid-state SIBs, and the facial designing and advanced characterizations for interfaces of all-solid-state SIBs, we put forward some view on the future development of inorganic SSEs.

2. Fundamentals of Na-ion SSEs

2.1. Mechanism of Na^+ transport in inorganic SSEs

Classical models describing Na-ion transport in SSEs treats ion leaps as uncorrelated and independent, which can be described as the transport of a single ion. Ion transportation can be achieved by hopping the mobile ions through various point defects, such as vacancies or interstitials [43,44]. The typical ion diffusion mechanism can be classified into three types: (1) Direct hopping mechanisms between vacancies; (2) direct hopping mechanisms between interstitials; (3) "knock-off" like mechanism between vacancies and interstitials (Figs. 1a-c). Within the crystal structure framework, individual ions are able to hop from one lattice site to another through connected diffusion channels, which is what is known as ion migration. The energy barrier for this ion transport process is determined by the framework. The highest energy along the diffusion pathway determines the energy barrier E_a of the mobile ion. However, the classical diffusion model contradicts the results of existing scientific research. He *et al.* reported that the ion transport mechanism is a multi-ion concerted migration mechanism for multiple adjacent ions hopping into their nearest sites simultaneously through AIMD simulations [43]. Increasing the Na concentration in SSEs yields high ionic conductivity. The low-energy sites in the structure of Na-ion conductors are preferentially occupied by Na-ions, while the excess Na-ions occupy the high-energy sites as the low-energy sites are fully occupied and cannot accommodate more Na-ions. In a multi-ion concerted migration process, Na-ions located at high-energy sites can effectively migrate downhill and cancel out some of the energy barrier that is felt by Na-ions occupying low-energy sites and undergoing upward migration. This results in lowered energy barriers for Na-ion diffusions (Fig. 1d).

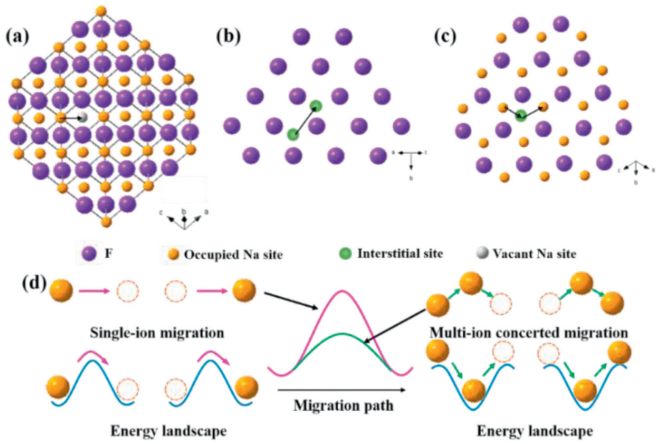

Fig. 1. Schematic diagram of four typical ion diffusion mechanisms of NaF, purple represents F ions, yellow represents occupied sodium ion sites, gray represents sodium ion vacancies, and green represents interstitial sites. (a) Direct hopping mechanisms between vacancies; (b) Direct hopping mechanisms between interstitials; (c) "Knock-off" like mechanism between vacancies and interstitials; (d) Conceptual diagram of the energy barriers required for single ion diffusion and multiple ions to diffuse in concert.

2.2. Crystal structures of various inorganic Na-ion SSEs

Inorganic Na-ion SSEs are a class of solid materials whose ionic conductivity are close to or exceeds that of the molten electrolyte. Two types of sublattices exist in the structure of SSEs. The first is a skeleton of non-moving ions that only undergo thermal vibrations with no ion transport, which cannot contribute to ion conduction in the structure. The second type consisting of the sublattice of mobile ions, which occupy the original lattice sites and undergo position shifts between other vacancies with similar activation energies, may provide a higher ion conductivity. Recently, inorganic Na-ion conductors can be classified into several types based on their compositions, such as oxides, sulfides, complex hydrides, and halides. The detailed crystal structure information of these different SSEs will be carefully summarized in the following parts of this section.

2.2.1. Na-β/β''-Al_2O_3

To date, Na-β/β''-Al_2O_3 stands as the sole commercially employed Na-ion SSE, finding primary applications in high-temperature sodium-sulfur batteries and solid-state SIBs [45–47].

Na-β/β''-Al_2O_3 exhibits a layered structure characterized by two-dimensional Na-ion conduction occurring between the layers. Fig. 2 illustrates the presence of two distinct crystal structures in Na-β/β''-Al_2O_3, denoted as Na-β-Al_2O_3 and Na-β''-Al_2O_3, respectively. The chemical composition of Na-β-Al_2O_3 is typically represented as $Na_2O(8–11)$ Al_2O_3. It adopts a hexagonal crystal system ($P6_3/mmc$) with lattice parameters $a = b = 5.58$ Å, $c = 22.45$ Å. Na-β-Al_2O_3 exhibits a stacking structure composed of two spinels [48–51]. The spinel layers adjacent to the Na-conducting layer are linked *via* O^{2-} within the Na-conducting layer, wherein the electrostatic attraction of O^{2-} to Na^+ is different in the two crystal structures.

Among them, the large electrostatic attraction of O^{2-} and Na^+ in Na-β-Al_2O_3 leads to a smaller unit cell volume, and the Na-conducting layer can accommodate less sodium ions, so it has a lower ionic conductivity. In contrast, the reduced electrostatic attraction between O^{2-} and Na^+ in the Na-β''-Al_2O_3 structure results in a larger unit cell volume compared to the Na-β-Al_2O_3 structure. Moreover, the Na-β''-Al_2O_3 structure exhibits a higher sodium ion content within the two-dimensional ion transport plane. These factors contribute to enhanced facilitation of sodium ion migration and consequently lead to higher ionic conductivity in

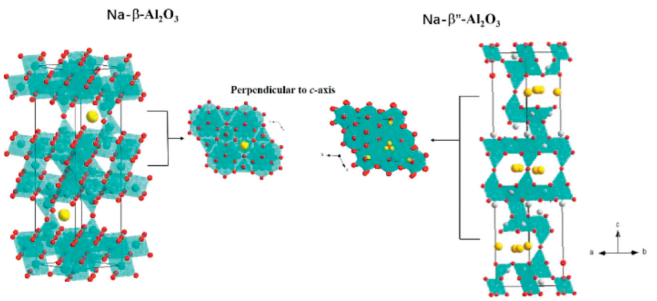

Fig. 2. Crystal structure of Na-β/β''-Al_2O_3. The yellow ball represents the sodium ion, the red represents the oxygen ion, and the gray represents the aluminum ion.

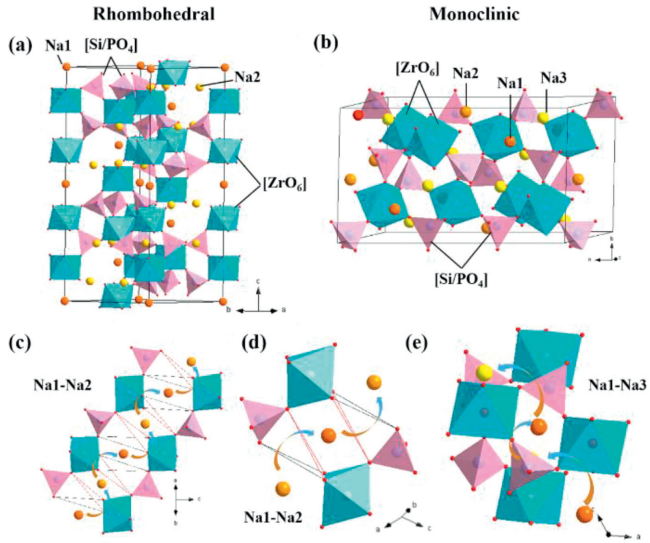

Fig. 3. Structures of Nasicon, different yellow balls represent different sites of sodium ions, red represents oxygen ion, blue octahedron represents [ZrO_6] octahedron, pink tetrahedron represents [Si/PO_4] tetrahedron: (a) Rhombohedral phase; (b) Monoclinic phase; (c) Na1-Na2 transport channel of rhombohedral phase; (d) Na1-Na2 transport channel and (e) Na1-Na3 transport channel of monoclinic phase.

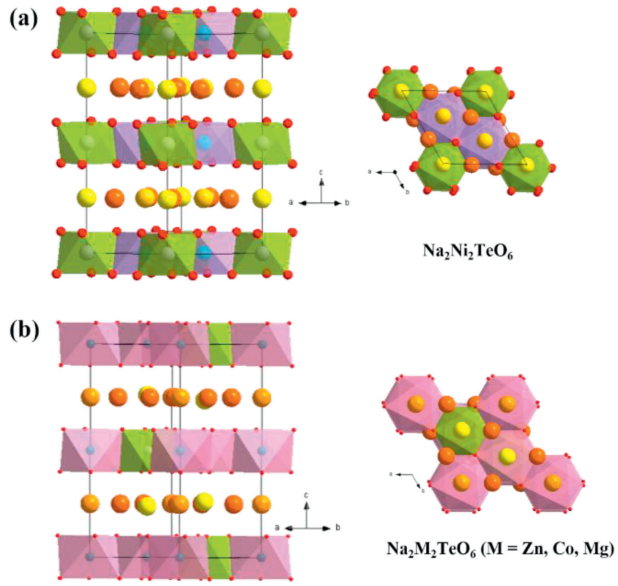

Fig. 4. Crystal structures of (a) $Na_2Ni_2TeO_6$ and (b) $Na_2M_2TeO_6$ (M = Zn, Co, Mg). Different yellow balls represent different sites of sodium ions, the green octahedron represents [TeO_6], the purple octahedron represents [NiO_6], and the pink octahedron represents [ZnO_6].

the Na-β''-Al_2O_3 structure. However, the thermodynamic stability of Na-β''-Al_2O_3 is relatively poor, posing challenges in obtaining a pure phase of this material. At high temperatures, Na-β''-Al_2O_3 is prone to decomposition into Al_2O_3 and Na-β-Al_2O_3. Moreover, the ionic conductivity of polycrystalline Na-β''-Al_2O_3 is influenced by the ratio between Na-β''-Al_2O_3 and Na-β-Al_2O_3 phases. Furthermore, Na-β''-Al_2O_3 exhibits greater sensitivity to moisture in the air and possesses inferior mechanical strength, thereby imposing additional constraints on its practical application.

2.2.2. Nasicon

Nasicon-type ($Na_{1+x}Zr_2Si_xP_{3-x}O_{12}$ $(0 \le x \le 3)$) SSE is another prominent class of Na-ion conductors that has received significant attention for its potential application in Na-ion SSEs. It was firstly proposed and studied by Goodenough and Hong in 1976 [37,38]. When $x = 2$, the composition $Na_3Zr_2Si_2PO_{12}$ exhibited remarkable ionic conductivity of 6.7×10^{-4} S/cm at r.t., 1.2×10^{-3} S/cm at 60 °C and 0.2 S/cm at 300 °C. In Nasicon-structured SSEs, two distinct crystal structures can be observed: a monoclinic structure (*C2/c*) within the compositional range of $1.6 \le x \le 2.2$, and a rhombohedral structure (*R-3c*). These crystal structures are illustrated in Figs. 3a and b, respectively. The monoclinic phase can transform into the rhombohedral phase upon heating to a temperature range of 420–450 K. The rhombohedral Nasicon structure exhibits a three-dimensional framework composed of corner-shared ZrO_6 and $(P/Si)O_4$ polyhedral units. Within this framework, Na-ions are situated and can be conducted isotropically within the rhombohedral Nasicon structure, there exist two crystallographically distinct Na-ion sites, denoted as Na1 and three Na2 sites. The monoclinic phase can be considered a distortion of the rhombohedral phase, whereby the structural units ZrO_6 and $(P/Si)O_4$ are remained during the distortion process but the overall symmetry of the structure is diminished. Furthermore, the structural distortion induces a modification in the occupancy of Na-ions, resulting in the division of the three Na2 sites into newly formed Na sites, namely one Na2 site and two Na3 sites. These additional Na-ion sites, created as a result of the distortion, serve as exchange sites for facilitating Na-ion transport. This phenomenon enhances the overall Na-ion mobility and promotes ion conductivity (Figs. 3c-e). In the monoclinic phase, the diffusion pathways for Na-ions include the Na1-Na2 channel and the Na1-Na3 transport channel. In contrast, the diffusion channel in the rhombohedral phase is primarily through the Na1-Na2 channel.

2.2.3. P2-type layered oxides

P2-type layered oxides are a new type of Na-ion SSE, which was first reported by Evstygneeva *et al.* in 2011 [39]. Four layered compounds, namely $Na_2M_2TeO_6$ (M = Ni, Co, Zn, Mg), were successfully synthesized and characterized, revealing their hexagonal crystal structures (Figs. 4a and b). $Na_2M_2TeO_6$ exhibits a honeycomb-like architecture, where each TeO_6 octahedron is surrounded by six MO_6 octahedra in the layers *via* edge-sharing interactions. Na-ions are located between layers occupying different positions, showing partial occupancy. The anisotropic conduction of Na-ions on the *ab* plane can be attributed to the limited permeability of Na-ions through the oxide layer. In this compound, three crystal graphically distinct Na-ion sites, denoted as Na1, Na2, and Na3, are present in each unit cell, with respective multiplicities of three, two, and one. And they have similar parameters of the hexagonal P2-type layered compounds: $a = 5.20$–5.28 Å, $c = 11.14$–11.31 Å, but different stacking sequences along *c*. In which $Na_2Mg_2TeO_6$ and $Na_2Co_2TeO_6$ were not obtain pure phases. And $Na_2Ni_2TeO_6$ exhibits a highest ionic conductivity of 10.1–10.8 S/m at 300 °C. However, its ionic conductivity can only reach 0.0008–0.0034 S/cm at r.t., which may be related to the generation of glass during the sintering process. The formation of glass phase increased its density, but the poor conductivity of the glass phase results in a high activation energy of up to 0.55 eV. Additionally, it is worth noting that the D-shells of the Ni and Co cations in the $Na_2Ni_2TeO_6$ and $Na_2Co_2TeO_6$ samples exhibit partial filling, and the oxidation state may undergo changes to enhance electronic conductivity. The measured electronic conductivity contribution of $Na_2Co_2TeO_6$, determined through the DC polarization method, is found to be only between 0.0031 S/cm and 0.0044 S/cm at 300 °C. Similarly, the electronic contribution of $Na_2Ni_2TeO_6$ is even lower. However, it should be noted that these materials may not be the optimal choices for SSEs due to the presence of variable valence elements such as Ni and Mn. During the charging and discharging process of the battery, redox reactions involving these elements can occur, resulting in electrolyte instability and self-discharge behavior of the battery.

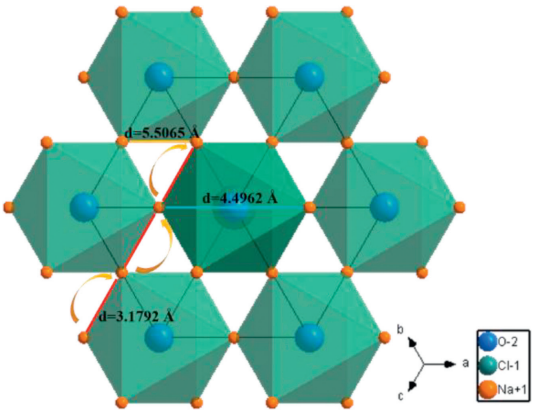

Fig. 5. Plan view of Na_3OCl along the [111] direction. Blue ball represents oxygen ion, green represents chloride ion, yellow represents sodium ion.

2.2.4. Anti-perovskites

Perovskites represent a class of structural types characterized by the connectivity of octahedra through shared vertices. From the perspective of structural chemistry, perovskites have a rich elemental composition, as well as a symmetrical diversity and a large number of symbiotic structures due to octahedral distortion. Anti-perovskites, being isostructural to perovskites, can be described by the general formula ABX_3, where the positive and negative ions occupy positions opposite to those in the perovskite structure [52,53]. Precisely, in perovskite structures, the A-site and B-site ions are cations, whereas the X-site is occupied by an anion, as exemplified by $CaTiO_3$. In contrast, anti-perovskites feature an arrangement where the A-site and B-site ions are anions, while the X-site is occupied by a cation, as observed in Na_3OCl (Fig. 5). On the one hand, in terms of crystal structure, anti-perovskites exhibit a comparable structural tolerance and diversity to perovskites. Additionally, in anti-perovskites, the oxygen ions are positioned at the center, while the larger A-site ions are situated at the face center of the cube, enabling jump-type ionic conduction. In recent years, Na-rich anti-perovskites demonstrated an exciting solution as a new class of ionic conductors [54–56]. These materials primarily consist of Na, O, and either Cl or Br, rendering them lightweight in nature. They exhibit favorable ionic conductivity and demonstrate excellent electrochemical stability towards Na. The anti-perovskite structure offers inherent flexibility and adjustability, facilitating chemical modifications aimed at enhancing the ionic conductivity.

2.2.5. Sulfide

Sulfide-based SSEs exhibit higher ionic conductivity and lower grain boundary impedance compared to oxide SSEs, owing to the larger atomic radius of sulfur (S) relative to oxygen (O). The introduction of S atoms in place of O atoms leads to lattice expansion and the formation of pathways conducive to Na-ion transport. Furthermore, the lower electronegativity of S compared to O results in a reduced binding capacity for Na-ions, facilitating their movement and thereby enhancing the overall ionic conductivity. Moreover, sulfide SSEs possess soft characteristics and can be synthesized at lower temperatures, eliminating the need for high-temperature ceramic sheet sintering required for oxide SSEs [57]. The powdered sulfide material can be cold-pressed to establish favorable electrode-electrolyte interfaces, simplifying the preparation process of solid-state batteries. However, it should be noted that sulfide SSEs exhibit poor stability and are susceptible to reaction with moisture in the air, leading to the release of toxic H_2S gas [58–60]. This limitation significantly hinders their application in practical settings.

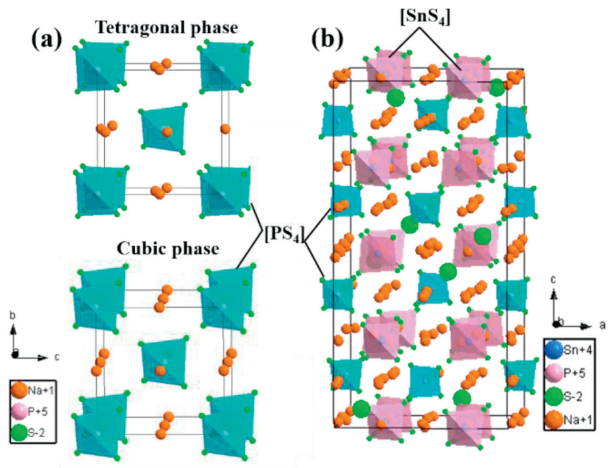

Fig. 6. Crystal structures of Na_3PS_4. (a) Tetragonal and cubic phase, (b) crystal structure of $Na_{11}Sn_2PS_{12}$. The blue ball represents tin ions, pink represents phosphorus ions, green represents sulfur ions, and yellow represents sodium ions.

Na_3PnS_4 (Pn = S, Sb): Na_3PS_4 exhibits two distinct crystal structures: tetragonal phase ($P\text{-}42_1c$; $a = b = 6.9520$ Å, $c = 7.0699$ Å) and cubic phase ($I\text{-}43$ m; $a = b = c = 7.0699$ Å). These two phases differ slightly in their structural arrangement. In the tetragonal phase, Na-ions distributed in one tetrahedral site and one octahedral site, while in the cubic phase, Na-ion is distributed in two distorted interstitial sites. The structure of Na_3PS_4 is shown in Figs. 6a and b. Among them, the conductivity of the cubic Na_3PS_4 is much higher than that of tetragonal Na_3PS_4, primarily attributed to their structural disparities. However, recent investigations have confirmed that the ionic conductivity of the tetragonal phase can also be higher than that of the cubic phase. In 2018, Takeuchi *et al.* synthesized tetragonal Na_3PS_4 with Na-rich vacancies by an improved preparation process [35], which had an ionic conductivity of 3.39×10^{-3} S/cm at 25 °C. This significant finding challenged the previously held notion regarding the ionic conductivity of the tetragonal and cubic phases. Subsequent theoretical investigations have further confirmed that the local structure of the two crystal forms of Na_3PS_4 does not exhibit noticeable differences. As a result, the disparity in crystal structure may not necessarily be a determining factor influencing its ionic conductivity. Instead, the variation in ionic conductivity could be attributed to the concentration of vacancies within the system.

$Na_{11}Sn_2PnSn_{12}$ (Pn = P, Sb; Sn = S, Se): In recent years, $Na_{11}Sn_2PS_{12}$ has emerged as a promising Na-ion conductor, garnering significant interest among researchers [61]. Zhang *et al.* first reported a $Na_{11}Sn_2PS_{12}$ electrolyte with a three-dimensional structure in 2017 [62]. Remarkably, this electrolyte demonstrated has an ionic conductivity of 1.4×10^{-3} S/cm at r.t. It is proved to be a new structure with space group $I4_1/acd$:2, $a = b = 13.6148(3)$ Å, $c = 27.2244(7)$ Å. The structural resemblance of $Na_{11}Sn_2PS_{12}$ to LGPS ($Li_{10}GeP_2S_{12}$) is evident (Fig. 6b). Within this framework, Na^+ are situated within octahedral sites, facilitating their transport along an interconnected three-dimensional pathway comprised of isoenergetic Na-S octahedra, which is further augmented by partial vacancy intersections. Notably, the ion transport pathway observed in $Na_{11}Sn_2PS_{12}$ represents the first instance of a fully three-dimensional faceted octahedral site pathway documented in sulfide SSEs.

2.2.6. Halide

The general formula for a sodium halide solid electrolyte is $Na_{3-x}M_{1-x}M'_xX_6$ (M can be a transition metal element, a lanthanide, a boron element, or a nitrogen element; M' can partially

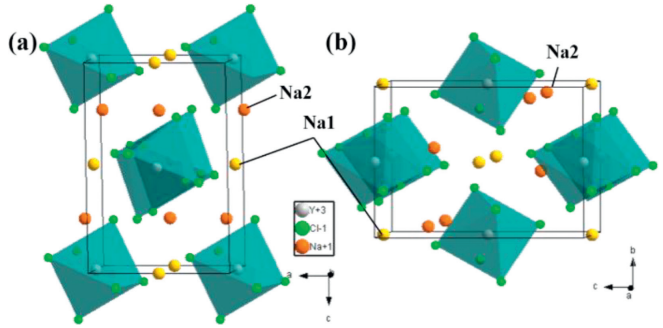

Fig. 7. Crystal structure of Na_3YCl_6. Different yellow balls represent different sites of sodium ions, the gray color represents yttrium ions and the green color represents chloride ions.

or completely replace Zr; X can be one or more halogens), and the radii of M and X determine the crystal structure of the material to some extent [44]. Common crystal structures include triangle *P31c*, triangle R-3, monoclinic crystal *P21/n* and monoclinic crystal *C2/m*. The crystal structure of the halide solid electrolyte is composed of stable NaX_6 and MX_6 octahedrons. The different NaX_6 connection modes determine the migration path of Na^+ and affect the conductivity of Na^+. For example, the $NaCl_6$ octahedra in Na_3YCl_6 are stacked face to face along the *c*-axis or side to side along the and axis. The former provides a fast migration path along the *c*-axis by directly migrating Na^+ from adjacent octahedral locations (Fig. 7).

2.2.7. Complex hydrides

Complex hydrides are a group of compounds composed of metal cations (*e.g.*, Na^+, Li^+) and complex anions ($[BH_4]^-$, $[B_{10}H_{10}]^{2-}$, $[B_{12}H_{12}]^{2-}$), which have received extensive attention due to their lighter weight, better electrochemical stability and excellent deformation properties. In 2012, Orimo *et al.* first presented the conduction of Na-ion in complex hydrides [63]. The ionic conductivity of $NaAlH_4$ was determined to be 2.1×10^{-10} S/cm, while that of Na_3AlH_6 was measured at 6.4×10^{-7} S/cm at r.t. Notably, the ionic conductivity of Na_3AlH_6 significantly increased to 4.2×10^{-4} S/cm at 433 K. The crystal structures of $NaAlH_4$ and Na_3AlH_6 are depicted in Figs. 8a and b, respectively. Although high ionic conductivity was not achieved in this study, it served as a significant milestone in exploring complexed hydrides as SSEs for Na-ions. Subsequently, they studied the $Na(BH_4)$-$Na(NH_2)$-NaI system [64]. The sample with the composition $Na(BH_4)_{0.5}(NH_2)_{0.5}$ exhibited the best ionic conductivity, reaching 2×10^{-6} S/cm. The excellent performance is attributed to its special anti-calcite structure, which has Na-ion vacancies and facilitates the transport of Na-ions. They believed that this material is promising for use in SIBs.

In 2014, Udovic *et al.* reported a novel complexed hydride SSE denoted as $Na_2B_{12}H_{12}$, this material exhibits an intriguing ordered-disordered phase transition, where the disordered phase driven by entropy becomes thermodynamically stable at elevated temperatures, enabling enhanced ion conduction kinetics. This unique phase behavior contributes to the fast transport of ions inside the material [65]. The two distinct structures of $Na_2B_{12}H_{12}$ are shown in Figs. 8c and d. The material is an ordered monoclinic phase at low temperature, while at higher temperatures, it undergoes a phase transition to a disordered body-centered cubic structure with a significant presence of cation vacancies. Notably, the disordered cubic $Na_2B_{12}H_{12}$ exhibits a remarkable enhancement in ionic conductivity, reaching up to 0.1 S/cm within the temperature range of 540 K to 573 K. However, the ionic conductivity of $Na_2B_{12}H_{12}$ at r.t. is not optimal, leading to a limited temperature range for its effective utilization as SSE.

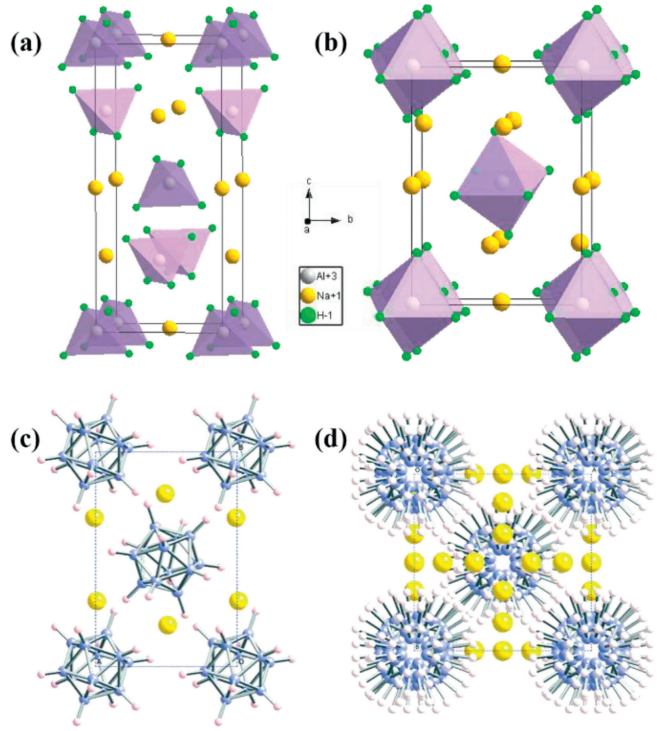

Fig. 8. Crystal structures of (a) $NaAlH_4$, (b) Na_3AlH_4, (c) low-temperature ordered monoclinic phase and (d) high-temperature disordered cubic phase. Reprinted with permission [65]. Copyright 2014, Royal Society Chemistry.

3. Synthesis methods for different sodium solid electrolytes

The processing of SSEs typically involves two main steps. The first step involves synthesizing substances that have a specific chemical composition, physical state, crystal structure, and desired properties. The second step involves fabrication of the SSE materials, such as shaping and fixing them through firing, sintering, filming, and other methods. However, with inorganic oxide SSEs, it can be difficult to give them desired shapes, forms, and sizes due to their inherent brittleness, which limits the types of fabrication methods that can be used. In contrast, sulfide materials like Na_3PS_4 are generally more deformable and can be shaped under local stresses. However, the specific synthesis method used can also affect the resulting ionic conductivity of the SSE.

For oxide SSE ceramics, the classical two-step processing method by solid-state reaction usually requires high temperature and long-time sintering, even higher than 1200 °C for several days sometimes. And high temperature is needed to facilitate the diffusion of the ions through the product layer. Therefore, increasing the surface area of reactants, preparing a homogeneous mixture of reactants, adding of impurities that can cause distortion in the crystal lattice and weaken the chemical bonds, *etc.* can promote the solid-state reaction. Additionally, metastable structure with higher formation energy comparing to stable one, such as Na-β''-Al_2O_3 comparing to Na-β-Al_2O_3, could exhibit high ionic conductivity. Introducing foreign ions or impurities stabilize such metastable structure is important for deigning SSEs with excellent Na-ion conduction. This part will describe in the following part.

Liquid-phase method is another commonly employed technique for synthesizing SSEs. Compared with the solid phase method, the power produced by the liquid-phase method is more uniform. This approach involves dissolving the raw materials in a suitable solvent, followed by a stirring-induced liquid-phase reaction and subsequent heat treatment. It is particularly useful for coating elec-

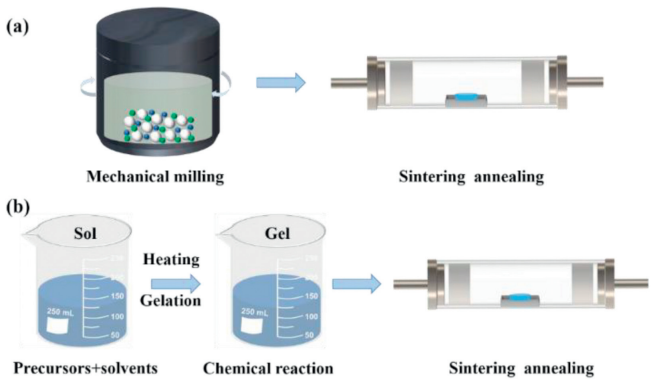

Fig. 9. Schematic diagram of synthesis of (a) solid state reaction and (b) liquid phase methods.

trode materials with electrolytes. However, when working with sulfide materials, caution must be exercised as they can undergo undesired side reactions with polar solvents. In Fig. 9, schematic diagrams depicting the synthesis processes using solid-state and liquid-phase methods are presented.

Na-β/β''-Al_2O_3 is generally synthesized using a conventional solid-phase method, which involves calcination at temperatures ranging from 1200 °C to 1250 °C, followed by sintering at 1600 °C. This method has been extensively studied due to its high yield and straightforward preparation process. However, this high-temperature sintering tends to lead to the loss of Na and the abnormal grain growth, which will weaken the materials and adversely affect its ionic conductivity. Furthermore, this method can produce $NaAlO_2$ at grain boundaries, which is hygroscopic and make Na-β/β''-Al_2O_3 susceptible to degradation. Therefore, Na-β/β''-Al_2O_3 prepared by solid-phase method is usually unstable. As a result, several methods including sol-gel synthesis, coprecipitation method, chemical vapor deposition and vapor-phase synthesis have proven to be effective alternatives to the traditional solid-state reaction. Shan *et al.* synthesized TiO_2 doped Na-β/β''-Al_2O_3 *via* a sol-gel method with tetrabutyl titanate (TBT) as the precursor for TiO_2 [66], the relative density reached 99.8%, this result showed that this method can accelerate grain growth and improve the densification. Butee *et al.* [67] synthesized Na-β/β''-Al_2O_3 by citrate sol-gel rote using glycerine as fuel, instead of ethylene glycol, and the synthesized Na-β/β''-Al_2O_3 has high density and high ionic conductivity. Virkar *et al.* [68] used Y-ZrO_2 and α-Al_2O_3 as raw materials and obtained dense ceramic sheets by a vapor phase process after high temperature sintering at 1450 °C for 17 h. Using this method can effectively enhance the chemical stability and mechanical strength of Na-β/β''-Al_2O_3.

The traditional solid-phase method has been the most commonly used approach for synthesizing Nasicon-type electrolytes, owing to its high yield and relatively simple preparation process. While the traditional solid-phase method is effective, it has some limitations, including the need for high temperatures (over 1200 °C) and long duration (over 20 h), which can result in abnormal grain growth and loss of Na and P during sintering. Additionally, poorly conducting ZrO_2 phases may be formed at grain boundaries due to the high sintering temperatures, leading to a decrease in ionic conductivity. Therefore, the density and the purity of the materials are the key to affect the ionic conductivity of the grain boundaries. A lot of works has been devoted to the synthesis of pure phase $Na_3Zr_2Si_2PO_{12}$. Naqash *et al.* synthesized Nasicon compositions with sodium excess, *i.e.*, $Na_3Zr_2Si_2PO_{12} + xNa_2O$ ($0 \le x \le 0.2$), demonstrated that the excess Na effectively compensated for the volatilized Na element at high temperature and effectively suppressed the formation of impurity of impurity phase [69]. The sample with $x = 0.2$ showed the least sodium deficiency and the highest ionic conductivity.

In addition, sol-gel method, hydrothermal method, solution-assisted solid-phase reaction (SASSR), liquid feed-flame spray pyrolysis (LF-FSP), spray freeze/freeze drying and low-temperature rapid microwave sintering method are also widely used to synthesize Nasicon materials with high densities. Compared with the traditional solid-phase method, sol-gel method can reduce the sintering temperature required for densification effectively, thus avoiding the formation of impurity phases. And the samples prepared by sol-gel method is more uniform than solid-phase method, therefore, this method is widely used for the synthesis of Nasicon electrolytes. Zhang *et al.* demonstrated that the sintering temperature could be reduced by the sol-gel method [70]. The results showed that the main phase of Nasicon prepared by sol-gel method was formed when sintered at 850 °C, and the sample obtained by sintering at 950 °C was well crystalline.

Solid phase reactions and liquid phase method are the main method for sulfide SSEs. Solid phase reaction involves high temperature sintering and annealing to obtain SSEs with a high degree of crystallinity. For sulfide SSEs, the sintering temperature is usually 200–800 °C. The liquid phase method involves dissolving various raw materials in a solvent to achieve homogeneous mixing of the reactants. The reduced particle size of the precursor powder shortens the mass transfer process, reduces the temperature of the reaction and densification and avoids the formation of tramp phases. A few typical examples of the preparation of sulfide electrolytes using different methods are given next.

In 2015, a cubic Na_3PS_4 SSE was firstly synthesized by liquid-phase reaction with NMF [71]. And its ionic conductivity was 2.6×10^{-6} S/cm. The presence of impurity Na_3POS_3 in the electrolyte made by this method is one of the reasons for the low ionic conductivity, the conductivity of the impurity phase is very low (about 10^{-8} order of order of magnitude), and the second reason may be due to the increase in R_{gb} leading to the decrease of conductivity. And changing the selecting compositions and solvents may improve ionic conductivity. Kim *et al.* synthesized Na_3SbS_4 using Na_2S, Sb_2S_3 and S as raw materials using the solution method, which used water as a solvent to avoid the reaction between organic solvents and sulfides [72].

4. Strategies for enhancing the conductivity and stability of Na-ion SSEs

The suitable SSE is crucial in the design of all-solid-state SIBs. An ideal SSE ought to have high ionic conductivity at r.t., electronic insulation, excellent electrochemical and interfacial stability. Among these characteristics, ionic conductivity stands out as the most significant performance parameter for SSEs. Consequently, extensive research works was devoted to enhancing the ionic conductivity of various electrolyte materials. Notably, sulfide SSEs are particularly sensitive to moisture and can undergo hydrolysis, releasing H_2S gas. Therefore, improving both the ionic conductivity and stability of sulfide SSEs is of utmost importance. Fig. 10 illustrates the reported conductivities of different inorganic sodium ion conductors, which are discussed in the subsequent sections.

4.1. Modification of Na-β/β''-Al_2O_3

The pure phase of Na-β''-Al_2O_3 is thermodynamically metastable, and upon heating to 1500 °C, it decomposes into Al_2O_3 and Na-β-Al_2O_3. Meanwhile Na-β''-Al_2O_3 is moisture sensitive with poor mechanical properties [73]. Ionic doping is commonly employed for stabilizing the Na-β''-Al_2O_3 phase. Zhu *et al.* discovered that after the introduction of Mg^{2+} and Li^+, the β"-Al_2O_3 content in the obtained samples was above 90% [74].

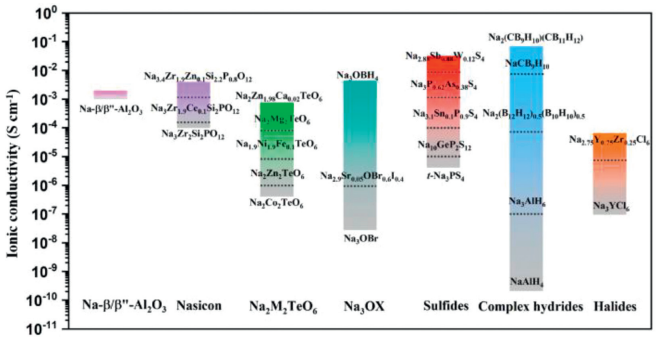

Fig. 10. Reported conductivities of Na-ion SSEs.

While the β''-Al_2O_3 phase content in the undoped samples was only 5%, which indicates that Mg and Li can stabilize the Na-β''-Al_2O_3 effectively, and it was also found that Mg^{2+} was more beneficial to improve the symmetry of Al(IV) in the Na-β''-Al_2O_3 phase than Li^+. Wei *et al.* examined the effects on the microstructure and electrical properties of Na-β''-Al_2O_3 by doping with TiO_2 [75]. The mechanical properties of the obtained samples were enhanced significantly with the increase of the doping amount, and the mechanical properties increased to more than 280 MPa when the TiO_2 content was higher than 1%. Xu *et al.* studied the influences of the Nb_2O_5 level to microstructure, mechanical performance and ionic conductivity of the Na-β''-Al_2O_3 [76]. They found that when the doping amount was 1 wt%, the Na-β''-Al_2O_3 phase content was 96.82%, the relative density could reach 98.93%. At the same time, the bending strength was also improved to 295 MPa. In addition to single ion doping, co-doping of multiple ions is also a common modification method. Yang *et al.* added a certain amount of TiO_2 and ZrO_2 when synthesizing Na-β''-Al_2O_3, in which ZrO_2-doped sample usually has high mechanical properties but poor electrical conductivity, while the TiO_2-doped sample usually high ionic conductivity [77]. Introducing Ti^{4+} and Zr^{4+} into Na-β''-Al_2O_3 could enhance ionic conductivity and mechanical performance. The synthesized sample with the addition of TiO_2 and ZrO_2 has improved bending properties up to 196.3 MPa with ionic conductivity of 0.2 S/cm at 350 °C. Moreover, dopants such as Li_2O [74], MnO_2 [78], MgO [79], NiO [80], CaO [49], ZrO_2 [81] and Y_2O_3 [68] have been shown to be effective in increasing the Na-β''-Al_2O_3 phase content as well as improving the mechanical properties.

4.2. Modification of Nasicon

The conduction mechanism of Na^+ within the grains and at the boundaries of Nasicon SSEs is different, therefore, efforts should be directed towards improving both the grain conduction and the grain boundary conduction to achieve overall enhancement in ionic conductivity.

4.2.1. Improve bulk conductivity

According to the Arrhenius equation, the ionic conductivity of the SSEs is proportional to $n_c \cdot \exp(-E_a/K_BT)$, where n_c is the concentration of Na-ions and E_a is the activation energy. It is evident that achieving higher ionic conductivity for a given temperature requires a low E_a and a high content (n_c) of Na-ions. The activation energy E_a is associated with the size of bottleneck through which the Na-ions must pass during transport. The size of this bottleneck determines the ease of Na-ion transportation. Consequently, the regulation of Na-ion concentration within the cell and the adjustment of the size of the three-dimensional transport channels for Na-ions represent the two primary approaches for enhancing ionic conductivity.

Nasicon type SSEs possess an open structure, and their ionic conductivity can be improved by optimizing their structure through element doping or chemical substitution. Early work mainly focused on the $NaZr_2(PO_4)_3$ system, after the replacement, the ionic conductivity was improved, but it was lower than $Na_3Zr_2Si_2PO_{12}$ [82–85]. Therefore, the current research is mainly to replace $Na_3Zr_2Si_2PO_{12}$. Based on the charge balance principle, the introduction of low-valence substitution in Nasicon-type SSEs leads to an increase in the concentration of Na^+ within the unit cell, which helps compensate for the positive charges resulting from the substitution. This can potentially enhance the ionic conductivity of the electrolyte. However, it is observed that the ionic conductivity does not always increase linearly with increasing doping amounts of low-valence ions. Experimental finds show that here exists an optimal doping level beyond which further increase in the dopant concentration actually leads to a decrease in the ionic conductivity. Theoretical calculations offer insights into this phenomenon by considering the maximum number of Na-ion occupancies within the unit cell, which is typically 4. The presence of sodium vacancies in the crystal structure is crucial for facilitating the movement of Na-ions. Therefore, when all the sodium vacancies are completely occupied, the available sites for Na-ions to jump between become limited. This saturation of sodium vacancies hinders the mobility of Na-ions and consequently results in a decrease in the overall ionic conductivity, even with higher dopant concentrations. After studying the composition of many electrolytes, the optimal concentration of Na per formula unit is around 3.3 mol [86]. And this conclusion was verified in subsequent reports. Ma *et al.* prepared $Na_{3+x}Sc_xZr_{2-x}Si_2PO_{12}$ by a solution-assisted solid-phase method, which provides a wide choice of starting materials and requires simple equipment suitable for large-scale preparation, and the relative densities of the samples in this work prepared by this method can reach 95% [87]. Results showed that the substitution will not only increase the concentration of Na-ions and decreases the phase transition temperature. The optimal ionic conductivity of the samples achieved 4.0×10^{-3} S/cm. Consequently, the introduction of low-valence ions such as Mg^{2+}, Zn^{2+}, Al^{3+}, and others has been demonstrated to be effective in increasing the ionic conductivity of these materials [88,89]. Nevertheless, it should be noted that certain elements with variable valence, such as Co, Fe, Cr, among others, are not suitable for doping in this particular system. The introduction of these elements may result in electrolyte instability and self-discharge of the battery [90].

In recent years, co-doping strategy have been widely investigated. By utilizing the synergistic effects of two different dopant ions, the co-doping approach can effectively further enhance conductivity. Typically, the two ions involved in co-doping contribute to the enhancement of ionic conductivity through different mechanisms. One of the ions usually adopts a lower valence to increase the Na-ion concentration within the unit cell. The other ion, with a larger radius, can widen the Na-ion transport channel or facilitate sintering to reduce the resistance at the boundaries. In addition, ions that decrease the temperature of phase transition can be selected as co-doping ions. He *et al.* a study on the Mg^{2+}/F^- co-doped $Na_3Zr_2Si_2PO_{12}$ strategy, aimed at enhancing the ionic conductivity of $Na_3Zr_2Si_2PO_{12}$ SSEs. In this strategy, Mg^{2+} and Zr^{4+} ions were chosen as co-dopants due to their identical radii (0.72 Å) [91]. As a result, Mg^{2+} doping increases the Na-ion concentration within the lattice without causing structural distortion. The introduction of F^- ions facilitates the enhancement of sintering activity in the ceramic material, leading to a gradual reduction of grain boundaries as well as a significant growth in material densities. Co-doping of Mg^{2+} and F^- ions resulted in an optimal ionic conductivity of 2.21×10^{-3} S/cm for the synthesized samples. Another ion commonly studied for co-doping is Sc^{3+}, which possesses a similar ionic radius to Zr^{4+} ($r(Zr^{4+}) = 0.72$ Å, $r(Sc^{3+}) = 0.745$ Å) but

a lower valence state. The incorporation of Sc^{3+} has been shown to effectively lower the phase transition temperature, making it a favorable co-doping ion. Omar *et al.* synthesized Sc/Yb co-doped $Na_3Zr_2Si_2PO_{12}$ SSEs [92]. The introduction of Sc^{3+} increases the concentration of Na-ions within the cell, while the introduction of Yb ions cause lattice expansion, which can broaden the size of Na-ion transport channels. In addition to co-substitution at the Zr site, simultaneous substitution at the Zr site and P is also effective in improving the ionic conductivity. Yang *et al.* simultaneously replaced part of the P with Si and part of the Zr with Zn to obtain $Na_{3.4}Zr_{1.9}Zn_{0.1}Si_{2.2}P_{0.8}O_{12}$ with an ionic conductivity of 5.27×10^{-3} S/cm [93]. The substitution of Zr with Zn in the SSEs expands the lattice due to the slightly larger radius of Zn compared to Zr. This expansion results in an increased bottleneck size of the Na1-Na-Na1 transport channel, which facilitates the transportation of Na-ions. Furthermore, the lower valence state of Zn ions contributes to an increased carrier concentration, leading to a ratio of Na-ion concentration to vacancy concentration of 3.4:0.6 within the system. This higher carrier concentration contributes to a higher ionic conductivity. The effectiveness of simultaneous Zr and P substitution has also been confirmed in other studies, such as the co-doping of P and Mg ions.

4.2.2. Decrease grain boundary resistance

The transport of ions at grain boundaries poses challenges due to the interruption of ion transport channels, leading to difficulties in ion diffusion. Consequently, the energy barrier for ion transport at grain boundaries is higher compared to the bulk material, resulting in lower ionic conductivity at the grain boundaries. The density and purity of the materials play crucial roles in influencing the ionic conductivity at grain boundaries. A lot of works has been devoted to the synthesis of pure phase $Na_3Zr_2Si_2PO_{12}$. Naqash *et al.* synthesized Nasicon compositions with sodium excess, *i.e.*, $Na_3Zr_2Si_2PO_{12} + xNa_2O$ $(0 \leq x \leq 0.2)$, demonstrated that the excess Na effectively compensated for the volatilized Na element at high temperature and effectively suppressed the formation of impurity of impurity phase [69]. The sample with $x = 0.2$ showed the least sodium deficiency and the highest ionic conductivity (1.6×10^{-3} S/cm at 25 °C).

In addition, sol-gel method, hydrothermal method, solution-assisted solid-phase reaction (SASSR), spray freeze/freeze drying and low-temperature rapid microwave sintering method are also widely used to synthesize Nasicon materials with high densities [94–99]. Sol-gel method can reduce the sintering temperature required for densification effectively, thus avoiding the formation of impurity phases. And the samples prepared by sol-gel method is more uniform than solid-phase method, therefore, this method is widely used for the synthesis of Nasicon electrolytes. Zhang *et al.* demonstrated that the temperature could be reduced by sol-gel method, results showed that the main phase of Nasicon prepared by sol-gel method was formed when sintered at 850 °C, and the sample obtained by sintering at 950 °C was well crystalline [70]. In addition, many novel preparation methods have also been used to prepare Nasicon materials. Ma *et al.* prepared $Na_{3+x}Sc_xZr_{2-x}Si_2PO_{12}$ by a solution-assisted solid-phase method, which provides a wide choice of starting materials and requires simple equipment suitable for large-scale preparation, and the relative densities of the samples in this work prepared by this method can reach 95% [87]. The optimal ionic conductivity of the samples achieved 4.0×10^{-3} S/cm.

The liquid phase sintering method is widely recognized as an effective approach to improve the density of materials. Oh *et al.* sintered NZSP in the Na_2SiO_3 with a melting point of 1088 °C, the formation of the melting pool of Na_2SiO_3 can improve the grain and grain boundary conductivity, and the highest ionic conductivity is 1.45×10^{-3} S/cm (Figs. 11a and b) [100]. Shao *et al.* employed NaF as a co-sintering agent in the sintering process to increase the density of Nasicon materials [101]. SEM images revealed that the ceramic sheet consisted of angular grains and "binder-like" amorphous glassy materials after NaF was added. This amorphous phase altered the grain boundaries, leading to an improvement in density and enhancing the ionic conductivity of $Na_3Zr_2Si_2PO_{12}$ from 4.5×10^{-4} S/cm to 1.7×10^{-3} S/cm (Fig. 11c).

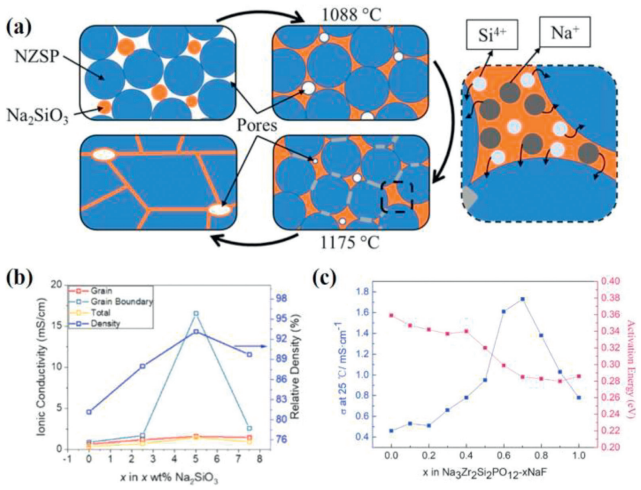

Fig. 11. (a) Schematic diagram of using $Na_2Si_2O_3$ as NZSP sintering additive and (b) ionic conductivity and relative density of these samples. Reprinted with permission [100]. Copyright 2019, American Chemical Society. (c) Ionic conductivity and E_a of samples with different levels of NaF. Reprinted with permission [101]. Copyright 2019, Elsevier.

4.3. Modification of layered oxides

As well as other types of SSEs, elemental doping is the main strategy commonly used to improve the ionic conductivity of layered oxide SSEs. Li *et al.* investigated Ga^{3+} doping on the structure and properties of $Na_2Zn_2TeO_6$ (NZTO) [102]. They found that a small amount of Ga^{3+} substitutes for Zn^{2+} would introduce more Na^+ vacancies in the interlayer gaps (Fig. 12a), which greatly reduce strong Na^+-Na^+ coulomb interactions and exhibit a superionic conductivity of 1.1×10^{-3} S/cm at r.t. Ga^{3+} doping improves the ionic conductivity significantly for the following reasons: (1) Ga^{3+} doping with smaller radius induces longer Na-O bonds and larger ion migration channels, which also reduces the attraction between Na^+ and O^{2-}; (2) Sufficient Na-site vacancies in NZTO-G0.1 not only increase the concentration of current carriers, but also reduce the migration energy of Na-ions. And the similar radii of Ga^{3+} and Zn^{2+} will not lead to distortion of the crystal structure. In 2018, Wu *et al.* analyzed the conduction of Na^+ in Ga^{3+}-doped $Na_2Zn_2TeO_6$ from the point of view defect chemistry for the first time [103]. The results indicate that the introduction of Ga^{3+} increases the concentration and mobility of mobile sodium ions, ultimately leading to an increase in the grain bulk conductivity. Furthermore, the existence of ZnGa defects with effective positive charges decreases the charge density in the space-charge layer, which reduces the Schottky barrier height, ultimately resulting in an increase in grain boundary conductivity (Figs. 12b and c). Ion doping with larger radius can also effectively improve the ionic conductivity. Deng *et al.* explored the effect of Ca^{2+} doping on the structure and properties of $Na_2Zn_2TeO_6$ [104]. The refinement results show that the unit cell parameters *a* and *c* and the distance between the two layers increase with the increase of Ca^{2+} doping content. At the same time, the ionic conductivity of $Na_2Zn_2TeO_6$ at r.t. is increased to 7.5×10^{-4} S/cm with the activation energy of 0.225 eV.

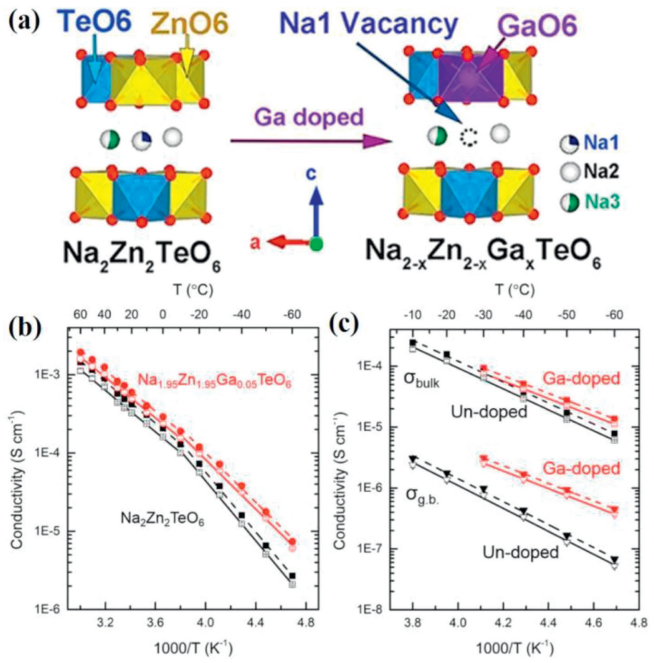

Fig. 12. (a) Transformation of partial crystal structure before and after Ga substitution in NZTO. Reprinted with permission [102]. Copyright 2018, Elsevier. (b) Total ionic conductivities of $Na_{1.95}Zn_{1.95}Ga_{0.05}TeO_6$ and $Na_2Zn_2TeO_6$ and (c) the σ_{bulk} and σ_{gb} of two samples at different temperatures Reprinted with permission [103]. Copyright 2018, Elsevier.

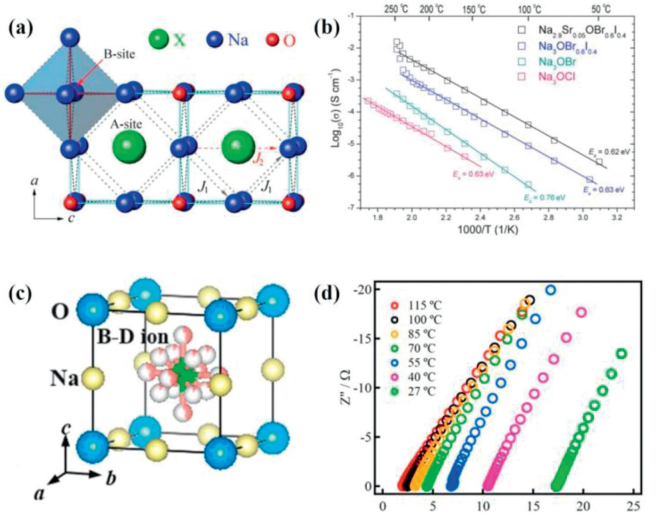

Fig. 13. (a) Crystal structure of Na_3OX (X = Cl, Br, I) and (b) Arrhenius plots for Na_3OCl, Na_3OBr, $Na_3OBr_{0.6}I_{0.4}$ and $Na_{2.9}Sr_{0.05}OBr_{0.6}I_{0.4}$ samples. Reprinted with permission [106]. Copyright 2015, Elsevier. (c) Crystal structure of Na_3OBD_4 and (d) Nyquist plots of hot-pressed Na_3OBH_4 pellet. Reprinted with permission [108]. Copyright 2019, American Chemical Society.

In addition to $Na_2M_2TeO_6$ (M = Ni, Co, Zn, Mg), Smaha *et al.* reported another layered Na ion conductor, $Na_{3-x}Sn_{2-x}Sb_xNaO_6$ (with a space group of *C2/c*) in 2015 [105]. This finding expanded the range of layered materials capable of facilitating sodium ion conduction. When $x = 0.8$, the maximum conductivity of $Na_{2.2}Sn_{1.2}Sb_{0.8}NaO_6$ at 500 °C is 1.43×10^{-3} S/cm and the activation energy is 0.63 eV. The authors believed that replacing Sn^{4+} with Sb^{5+} would create Na vacancies and thus promote higher Na-ion mobility.

4.4. Modification of anti-perovskites

Modulation of local structural features by elemental doping or creating vacancies is a common way to improve ionic conductivity. In 2015, Wang *et al.* synthesized Na_3OCl and Na_3OBr with anti-perovskite structure, and found that the ionic conductivity of Na-rich anti-perovskite can be improved by changing the element species at the halogen site and creating Na-ion vacancies (Fig. 13a) [106]. The $Na_3OBr_{0.6}I_{0.4}$ obtained by introducing I^- into Na_3OBr possesses the highest ionic conductivity of 0.43 mS/cm at 200 °C. The sodium ion conductivity increases sequentially from Na_3OCl to Na_3OBr to $Na_3OBr_{0.6}I_{0.4}$, which proves that the mismatch effect caused by the incorporation of larger halide ions at the A site can improve the ionic conductivity. Then high-valence Sr^{3+} are doped into Na sites to introduce Na vacancies, and the obtained $Na_{2.9}Sr_{0.05}OBr_{0.6}I_{0.4}$ has an ionic conductivity of 19 mS/cm at 200 °C. This work confirms that unequal alkaline earth mental ion doping can enhance the ionic conductivity of anti-perovskite SSEs effectively. On the other hand, the free transport volume in the anti-perovskite structure can also be changed by modifying the anions on the A-site. And the free space in the anti-perovskite structure depends on the size of the anion once the rigid backbones are fixed. Larger anions will leave a smaller free space in the framework. Therefore, the A site preferentially selects anions with smaller radii. But if the anion at A-site is too small to fill the cavity, it will cause the anti-perovskite structure to collapse or distorted, leaving little free space for ion migration. This work showed the benefit of cation mixing in anti-perovskite electrolytes with the Na_3OBr and $Na_3OBr_{0.6}I_{0.4}$ samples, substituting the smaller A anion with a larger anion may maintain the general formula of free space to provide a stable structure, thus, the activation energy of the mixed cation sample is much lower than that of a single cation (0.63 eV for $Na_3OBr_{0.6}I_{0.4}$ and 0.76 eV for Na_3OBr), as shown in Fig. 13b. To further improve the conductivity, researchers are focusing their attention to anion groups. Substituting X with a cluster (*i.e.*, $Na_3S(BCl_4)$ and $Na_3O(BF_4)$) was predicted to be an effective way to achieve higher ionic conductivity [107]. In 2019, Sun *et al.* synthesized Na_3OBH_4 with an anti-perovskite structure by solid-phase method (Fig. 13c) [108]. Its ionic conductivity is 4.4×10^{-3} S/cm, which is four orders of magnitude higher than the existing Na_3OX (X = Cl, Br, I) (Fig. 13d). The synthesis of Na_3OBH_4 with higher ionic conductivity may be an important advance in the development of Na-rich anti-perovskite electrolytes. Gao *et al.* synthesized Na_3ONO_2 by a low temperature solid-state reaction, ESI measurements showed that the highest ionic conductivity in Na_3ONO_2 (0.37 mS/cm, E_a: 0.385 eV) around 485 K [109]. And they used Neutron powder diffraction refinements and DFT calculations reveal the mechanism of the conductivity enhancement. Above 485 K, the NO_2^- rotation is more intensified than that at lower temperature, which can significantly facilitate Na^+ ion migration *via* Na–O interactions.

In addition, a large amount of theoretical computational work has driven the development of Na-rich anti-perovskite materials. Wan *et al.* studied the effect of substitutional defects on the Na migration energy through NEB computations and AIMD simulations [110]. They investigated the effects of divalent and trivalent dopants (Mg^{2+}, Ca^{2+}, Sr^{2+}, Ba^{2+}, Al^{3+}, and Ga^{3+}) on the ionic transport and conductivity in Na_3OCl, the results showed that Ba is the most stable substitutional defect among the ones studied. It was also found that Ca^{2+} may be the most potential doped ion because it leads to the lowest dopant-vacancy binding energy. Goldmann *et al.* investigated the cation doping mechanisms and ionic conductivity in the anti-perovskite Na_3OCl in an atomic-scale perspective [111]. They found that the most favorable aliovalent cation dopants are Mg^{2+}, Ca^{2+}, Al^{3+} and Ga^{3+} with Na-vacancy charge compensation; an increase in Na-vacancy concentration would promote Na-ion conductivity. The highest conductivity is found for the

Mg-doped system of the order of 10^{-5} S/cm at 500 K, but lower conductivities are predicted for the trivalent Al and Ga dopants.

Currently, there is a limited variety of Na-rich anti-perovskite SSEs available, and their ionic conductivity at r.t. does not meet the requirements for practical applications. Correspondingly, the development of all-solid-state SIBs utilizing these electrolytes is still limited. Therefore, it is crucial to actively explore new types of anti-perovskite materials in order to expand the range of Na-ion SSEs options. Additionally, there is a need to investigate alternative preparation methods for anti-perovskite electrolytes. For instance, in the case of Na_3OBH_4 mentioned earlier, the author demonstrated that hot-pressing sintering method yielded significantly higher ionic conductivity (4.4×10^{-3} S/cm) at r.t. compared to samples prepared using the traditional cold-pressed sintering method [108]. This also shows that the preparation process of the sample has a great influence on its performance. Furthermore, anti-perovskite SSEs should be studied from multiple perspectives. Previous studies on F ion conductors and O ion conductors have shown that the ability of ion conductivity can be regulated by controlling the pressure, while the effect of pressure on the ionic conductivity of Na-rich anti-perovskite materials has not been investigated [112,113]. In 2016, Wang *et al.* invested the structure stability of anti-perovskite Na_3OBr and Na_4OI_2 SSEs under high pressure by *in-situ* SR-XRD [114]. The results demonstrate that both the cubic Na_3OBr structure and tetragonal Na_4OI_2 structure remain stable under high pressure conditions up to 23 GPa. However, it should be noted that the variation of ionic conductivity of anti-perovskites as a function of pressure has not been reported.

4.5. Modification of sulfide SSEs

4.5.1. Improve ionic conductivity

Na_3PnS_4 (Pn = P, Sb): Element doping is a widely employed approach to enhance the ionic conductivity of Na_3PS_4 materials. The effect of doping ions on the ionic conductivity can be attributed to several factors, including following aspects. On the one hand, low-valence ions such as Sn^{4+}, Ge^{4+}, Ti^{4+}, replace P^{5+} ions, in order to maintain the overall electrical neutrality, excess Na-ions are often introduced, which is beneficial to reduce the activation energy and improve the conductivity of Na-ions. Replacing S^{2-} with low-valent anions such as F^-, Cl^-, Br^- can introduce more Na-ion vacancies, increase the effective hopping probability of Na-ions between adjacent sites, and thus improve the ionic conductivity. On the other hand, ionic doping with larger radius (such as As^{5+}) expands the lattice and elongates the Na-S bonds, thereby increasing the ionic conductivity. We summarize the modification methods of Na_3PnS_4 (Pn = P, Sb) solid electrolyte according to the different doping sites.

In 2014, Tanibata *et al.* reported for the first time (100-x) Na_3PS_4·xNa_4SiS_4 glass-ceramic, in which the glass-ceramic containing 6% Na_4SiS_4 had an ionic conductivity of 7.4×10^{-4} S/cm at r.t. [115]. And it was found that the introduction of Si ions caused excess Na ions to occupy Na2 sites, which is also the reason for the improvement of its ionic conductivity. In 2019, Hayashi *et al.* reported the W-doped Na_3SbS_4 solid electrolyte $Na_{2.88}Sb_{0.88}W_{0.12}S_4$, the ionic conductivity can reach 3.2×10^{-2} S/cm at r.t. [116]. Because of the ionic radius of Sb is larger than that of P, and replacing P with Sb can effectively expand the ion transport channel and achieve higher ionic conductivity (Figs. 14a and b) [33,117,118]. Yu *et al.* replaced a part of P ions in Na_3PS_4 with As^{3-} ions, and synthesized a solid electrolyte composed of $Na_3P_{0.62}As_{0.38}S_4$, with a high ionic conduction of 1.46×10^{-3} S/cm at r.t. [119]. Weng *et al.* synthesized WS_2 -doped $Na_{3-x}Sb_{1-x}W_xS_4$ and WO_2-doped $Na_{3-x}Sb_{1-x}WxS_{4-2x}O_{2x}$ ($x = 0.025, 0.05, 0.075, 0.1$) solid electrolytes, The room temperature ionic conductivity of the sample composed of $Na_{2.95}Sb_{0.95}W_{0.05}S_4$ and $Na_{2.95}Sb_{0.95}W_{0.05}S_{3.9}O_{0.1}$ can achieve 10.37 and 8.49 mS/cm [120].

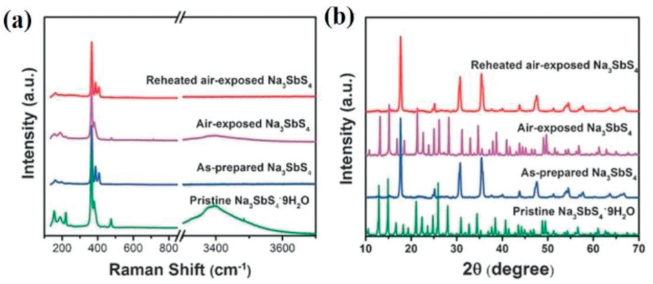

Fig. 14. (a) Raman spectra and (b) XRD patterns of Pristine $Na_3SbS_4·9H_2O$, as-prepared Na_3SbS_4, air-exposed Na_3SbS_4 and reheated air-exposed Na_3SbS_4. Reprinted with permission [33]. Copyright 2016, Wiley Online Library.

Equivalent doping has been shown to be effective in enhancing ionic conductivity. In 2015, Zhang *et al.* replaced S with Se lead to Na_3PSe_4 with an ionic conductivity of 1.16×10^{-3} S/cm, and reduced the *Ea* of the electrolyte to 0.21 eV [121]. The increase of ionic conductivity could result from two factors, firstly, the substitution of Se^{2-} with larger ionic radius for S^{2-} can expand the lattice; Second, Se^{2-} with greater polarizability will weaken the binding energy between Na ions and S^{2-} framework, thereby improving the mobility of Na ions. Ceder *et al.* combined theoretical calculations and experiments to study the Na^+ conduction mechanism in cubic Na_3PSe_4 [122]. The study found that when Na_3PSe_4 has defects, it is conducive to the rapid conduction of Na^+, indicating that the mechanism of ion transport in Na_3PSe_4 is vacancy transport mechanism.

Guided by first-principles calculations, Chu *et al.* synthesized a series of novel Cl-doped tetragonal Na_3PS_4 (t-$Na_{3-x}PS_{4-x}Cl_x$) samples by solid phase reactions [123]. The various reaction materials were ground, calcined, reground and re-pelletized. These pellets were then treated by spark plasma sintering. The sample with the composition $Na_{2.9375}PS_{3.9375}Cl_{0.062}$ exhibited the highest ionic conductivity of 1.0×10^{-3} S/cm at r.t., and the assembled full cell displayed reversible charging and discharging at a rate of 0.1 C. The researchers demonstrated, using density functional theory calculations, that the exceptional performance of the Cl-doped Na_3PS_4 electrolyte in this battery can be attributed not only to the high conductivity of Na-ions in the SSEs but also to the formation of an electronically insulating and ionically conductive interface layer at the electrode-electrolyte interface due to the presence of Cl^-.

In 2018, Moon *et al.* synthesized Ca-doped Na_3PS_4 by the solid-phase method, found that Na^+ in t-Na_3PS_4 was replaced by Ca^{2+}, forming a cubic phase of $Na_{3-2x}Ca_xPS_4$, and at the same time generating Na^+ vacancies, which greatly improved the ionic conductivity. When $x = 0.135$, it can reach 1×10^{-3} S/cm at 25 °C [124].

$Na_{11}Sn_2PnSn_{12}$ (Pn = P, Sb; Sn = S, Se): In 2018, Duchardt *et al.* replaced the S atom in $Na_{11}Sn_2PS_{12}$ with Se to obtain an electrolyte with a composition of $Na_{11.1}Sn_{2.1}P_{0.9}Se_{12}$ [125]. Its performance test found that the ionic conductivity was almost unchanged before and after Se substitution, but the activation energy decreased significantly after substitution ($Na_{11}Sn_2PS_{12}$: 0.39 eV and $Na_{11.1}Sn_{2.1}P_{0.9}Se_{12}$: 0.30 eV). Structural analysis shows that the substitution of Se atoms with larger radii for S atoms can broaden the ion transport channel, and the substitution of Se for S makes the lattice softer, lowering the migration barrier for ion transport in the lattice, thereby lowering the activation energy. In 2020, Jia *et al.* reported a halogen ion-doped $Na_{3.67}[Sn_{0.67}Si_{0.33}]_{0.67}P_{0.33}S_4$ electrolyte, in which $Na_{3.57}[Sn_{0.67}Si_{0.33}]_{0.67}P_{0.33}S_{3.9}I_{0.1}$ was obtained by I^- doping [126]. The ionic conductivity of the electrolyte can reach 1.08×10^{-3} S/cm at r.t. Structural studies show that doping I with a larger radius than S can expand the lattice and accelerate the transport of Na ions. In 2021, Liu *et al.* synthesized a new type of solid electrolyte $Na_{10}SnSb_2S_{12}$, which showed a room tempera-

ture ionic conductivity of 0.52 mS/cm and a low activation energy of 0.23 eV [14].

4.5.2. Chemical and electrochemical stability

Despite the achievement of practical RT ionic conductivity in sulfide SSEs, their sensitivity to moisture and air remains a significant challenge that hinders their widespread application. The instability of sulfide SSEs in the presence of moisture and air can be explained by the "theory of hard and soft acids and bases". According to this theory, there is a preference for the interaction between hard acids and hard bases, as well as soft acids and soft bases. In the case of sulfide SSEs, S^{2-} acts as a soft acid and tends to bind with soft bases to form stable structures. On the other hand, P^{5+} acts as a hard acid and tends to bind with hard bases such as O^{2-}. Consequently, most P-based sulfide SSEs exhibit lower stability in the presence of air. However, Na_3SbS_4, which contains Sb^{5+} as a soft acid, exhibits improved chemical stability. Wang *et al.* investigated the air stability of Na_3SbS_4 and observed the formation of $Na_3SbS_4{\cdot}9H_2O$ when exposed to air, as indicated by Raman and XRD results (Figs. 14c and d). Nevertheless, after sintering at 150 °C for 1 h, Na_3SbS_4 returned to its original form, demonstrating excellent chemical stability in air [33]. In addition to this, partial substitution of P in Na_3SbS_4 with As and Sn also had a significant effect on its chemical stability [119,127].

The electrochemical stability of sulfide SSEs is typically assessed using cyclic voltammetry, where inert electrodes are used as blocking electrodes and Na metal is used as the counter electrode. The electrochemical window, which indicates the range of stable electrochemical potentials, is an important parameter for evaluating the stability of solid electrolytes. For instance, Na_3PS_4 has been reported to have an electrochemical window of stability up to 5 V (*vs.* Na^+/Na) as measured by cyclic voltammetry. However, experimental studies have shown that Na_3PS_4 is not stable when in contact with the Na negative electrode. Yue *et al.* conducted tests on the Na-Sn-C|Na_3PS_4|Na_3PS_4-Na_2S-C system and observed the oxidation of Na_3PS_4 at approximately 2.0 V during the first charge. This finding indicates that the actual electrochemical stability window for sulfide electrolytes may be less favorable than the results obtained from cyclic voltammetry tests. Therefore, it is crucial to consider the actual electrochemical behavior and stability of sulfide electrolytes under specific operational conditions, particularly in contact with the negative electrode, to ensure their reliable performance in practical applications.

Sodium metal possesses a high energy density, but its reactivity poses challenges for achieving stable interfaces with electrolyte materials. The stability of the electrolyte in relation to sodium metal plays a crucial role in determining the formation of a stable interface. When the electrolyte is thermodynamically stable relative to sodium metal, a stable interface is formed upon contact. Conversely, if the electrolyte is thermodynamically unstable, rapid chemical reactions occur, leading to an increase in interfacial impedance, a decrease in ion diffusion rate, and ultimately, the failure of the cell. To enhance the electrochemical stability of sulfide SSEs, it is essential to design electrolyte materials and interfaces in a rational manner. One approach involves the doping of Cl^- ions into Na_3PS_4, as demonstrated by Chu *et al.* This Cl^- doping can passivate or stabilize the electrode-electrolyte interface, thereby improving the electrochemical stability of the electrolyte [123]. By carefully modifying the composition and structure of the electrolyte, it is possible to achieve improved stability and performance in sulfide solid electrolyte-based systems. Such strategies for enhancing electrochemical stability are crucial for enabling the practical application of sulfide solid electrolytes, ensuring their long-term performance and reliability in advanced energy storage devices.

4.6. Modification of halide SSEs

In 1995, Mathias *et al.* reported Na_3MX_6 (X = Cl, Br) SSEs for the first time [128]. Na_3SmBr_6 and Na_3GdCl_6 showed an ionic conductivity of only 10^{-5} S/cm, while Na_3YbBr_6 and Na_3YbCl_6 showed an even lower ionic conductivity of 10^{-6} S/cm. Such low ionic conductivity renders them unsuitable for applications in all-solid-state SIBs. In recent years, Li-ion halides (Li_3YCl_6, Li_3YBr_6, Li_2ZrCl_6) have been reported as promising Li-ion conductors [129–133]. The outstanding properties of high ionic conductivity at r.t. and excellent chemical and electrochemical stability have garnered significant interest in the study of lithium-ion conductors. While Li_3YCl_6 and Li_3YBr_6 have been extensively investigated, sodium halides such as Na_3YCl_6 and Na_3YBr_6 have received comparatively less attention. This is attributed to the fully occupied 2d and 4e sites in Na_3YCl_6 (NYC) (space group: $P2_1/n$), which restrict ion hopping and consequently result in lower ionic conductivity. In 2021, Wu *et al.* addressed this limitation by introducing high-valence Zr^{4+} doping to create sodium vacancies, thereby improving the ionic conductivity of these materials [134]. They synthesized a series of Zr^{4+}-doped $Na_{3-x}Y_{1-x}Zr_xCl_6$ samples, remarkably, the introduction of Zr^{4+} doping led to a substantial improvement in r.t. ionic conductivity. When $x = 0.75$, the doped sample exhibited an impressive ionic conductivity of 6.6×10^{-5} S/cm, which is three orders of magnitude higher compared to the undoped sample.

Recently, Zhang *et al.* synthesized a Na_3YbCl_6-based halide electrolyte using high-energy ball milling, and the optimized $NaYbZrCl_{0.75}$ sample has a high ionic conductivity of 6.6×10^{-5} S/cm and a wide electrochemical window of 4.1 V [135]. Xu *et al.* synthesized a series of F-doped $NaAlCl_{4-x}F_x$ ($x = 0$, 0.1, 0.3, 0.5, and 0.7) and borohydride (BH_4)-doped $NaAlCl_{4-x}(BH_4)_x$ ($x = 0.1$ and 0.3) halide solid electrolytes using a straightforward ball-milling method, and these samples maintained the same orthorhombic structure as $NaAlCl_4$ [136]. The Na^+ conductivity of the appropriately doped $NaAlCl_{4-x}F_x$ SEs was found to be higher than that of $NaAlCl_4$. Specifically, $NaAlCl_{3.3}F_{0.7}$ exhibited significantly enhanced Na^+ conductivity (3.56×10^{-5} S/cm at 30 °C) compared to $NaAlCl_4$ (4.14×10^{-6} S/cm at 30 °C). Fu *et al.* developed a new class of halide heterogeneous structure electrolytes by exploiting the structural differences between high and low coordination halide frameworks [137]. Halide heterogeneous structure electrolytes containing UCl_3-type high coordination frameworks and amorphous low coordination frameworks achieved a Na^+ conductivity of 2.7 mS/cm at room temperature. Recently, Hu *et al.* successfully designed and synthesized a novel amorphous $NaTaCl_6$ halide solid-state electrolyte that exhibits an ultra-high ionic conductivity of 4×10^{-3} S/cm at room temperature [138]. The excellent ionic conductivity achieved can be attributed to the formation of a reconfigured amorphous poly($TaCl_6$) octahedral network triggered by high-energy mechano-chemical reactions, which efficiently drives sodium ions into the open amorphous halide network, resulting in weaker Na-Cl interactions.

4.7. Modification of complex hydrides

Among the reported composite hydride solid-state electrolytes, $Na_2B_{12}H_{12}$ in its disordered phase has been found to exhibit the highest ionic conductivity at elevated temperatures. Consequently, recent investigations in complex hydrides have aimed to reduce the phase transition temperature of $Na_2B_{12}H_{12}$. In 2015, Tang *et al.* reported that the ionic modifications can effectively lower the phase transition temperature [139]. They replaced B in $Na_2B_{12}H_{12}$ with C atom to form $NaCB_{11}H_{12}$ (Figs. 15a and b), and found that the material had a phase transition of 308 K (600 K for $NaCB_{11}H_{12}$) and an ionic conductivity of 0.12 S/cm at 383 K. Battaglia *et al.* mixed two precursors of $Na_2B_{12}H_{12}$ and $Na_2B_{10}H_{10}$ in a ratio of

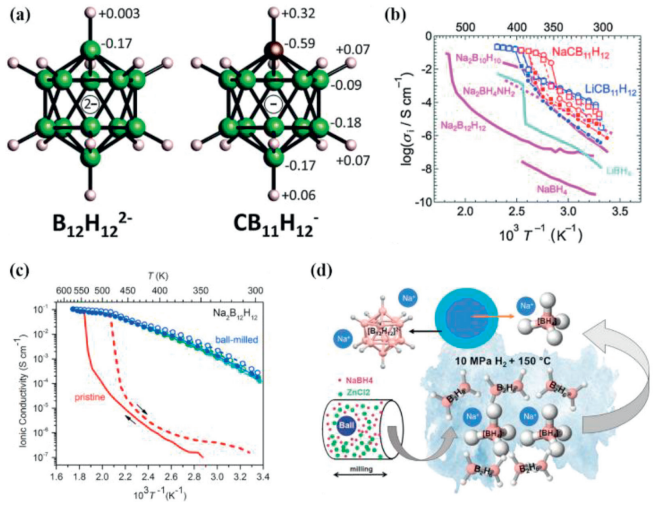

Fig. 15. (a) Structure diagram of $B_{12}H_{12}^{2-}$ and $CB_{11}H_{12}^{-}$. (b) The ionic conductivities of Li^+ and Na^+ species in $LiCB_{11}H_{12}$ and $NaCB_{11}H_{12}$ were measured as a function of inverse temperature. Reprinted with permission [139]. Copyright 2015, RSC publishing. (c) The ionic conductivity of pristine and ball-milled $Na_2B_{12}H_{12}$ was compared after QENS measurements. Reprinted with permission [141]. Copyright 2016, Elsevier. (d) A description of the synthetic route of $NaBH_4$@$Na_2B_{12}H_{12}$. Reprinted with permission [142]. Copyright 2022, American Chemical Society.

1:1 to obtain $Na_2(B_{12}H_{12})_{0.5}(B_{10}H_{10})_{0.5}$ electrolyte, and the ionic conductivity of the material reached 0.9 mS/cm at 20 °C [140]. XRD and DSC characterizations showed that this compound has a face-centered cubic structure at r.t. (the same as that of $Na_2B_{12}H_{12}$ at 180 °C), which also confirmed that anion doping can effectively reduce the phase transition temperature.

The ball-milling method has demonstrated effectiveness in reducing the phase transition temperature of $Na_2NH_2B_{12}H_{12}$. Tang *et al.* observed that this method, through the reduction of crystallite size and induction of disordering effects, leads to the stabilization of a high-temperature-like superionic-conducting phase at r.t. [141]. The effectiveness of the high-temperature disordered phase was further substantiated through XRD and other characterization techniques. Performance testing also revealed a significant improvement in the ionic conductivity of the ball-milled samples (Fig. 15c). Furthermore, the synthesis of mixed anionic hydrides has demonstrated its efficacy in reducing the phase transition temperature.

In 2022, Luo *et al.* successfully synthesized a novel solid-state electrolyte, $NaBH_4$@$Na_2B_{12}H_{12}$, featuring a distinct core-shell structure (Fig. 15d) [142]. The sample exhibited a high ionic conductivity of 10^{-4} S/cm at 115 °C. The results showed that the core-shell structure may facilitate $NaBH_4$/$Na_2B_{12}H_{12}$ interfacial sites for sodium ion hopping. This, in turn, improves the ionic conductivity, providing a novel approach for enhancing the ionic conductivity of complex hydride SSEs.

The primary objective of developing SSEs is to successfully apply them to solid-state batteries, achieving superior safety, high energy/power density, and extended cycling performance. In this section, we will provide a comprehensive overview and analysis of the current state of solid sodium batteries based on the aforementioned SSE.

5. Solid-state batteries applications for Na-ion SSEs

The primary objective of developing SSEs is to successfully apply them to SIBs, achieving superior safety, high energy/power density, and extended cycling performance. In this section, we will provide a comprehensive overview and analysis of the current state of SIBs based on the aforementioned SSEs.

5.1. Solid-state SIBs based on oxide SSEs

Na-β''-Al_2O_3, renowned for its remarkable ionic conductivity, has emerged as a pioneering SSE for sodium batteries [143]. ZEBRA batteries and high-temperature Na-S batteries were discovered based on it. Its operating temperature is generally around 300 °C, which not only increases the operational and maintenance costs of the battery but also increases safety hazards [144–146]. Due to the low room temperature ionic conductivity of Na-β-Al_2O_3, large grain boundary impedance, and poor sodium affinity, it cannot work at lower temperatures [147]. To reduce the operating temperature of Na-β-Al_2O_3-based batteries, it is necessary to enhance the room temperature ionic conductivity of Na-β-Al_2O_3 electrolytes, and to improve the solid-solid contact interface between the electrolyte and electrode materials. Recently, there has been emerging research on solid-state SIBs utilizing Na-β''-Al_2O_3 electrolytes, which exhibit promising performance even at ambient temperature. Zhao *et al.* used a strip casting and sintering process to prepare Na-β''-Al_2O_3 thin films with a thickness of about 100 μm [148]. The battery used gel $NaTi_2(PO_4)_3$ as the cathode and Na metal the anode. The reversible discharge capacity remained at 100 mAh/g after 50 cycles (Fig. 16a). Na-β''-Al_2O_3 is highly stable with Na and has a wide electrochemical window. Nevertheless, the inadequate interface contact between the Na metal anode and electrolyte leads to elevated interfacial resistance and non-uniform Na^+ deposition [13,149]. To address these issues, Wen *et al.* proposed a dual-functional layer composed of three-dimensional cross-linked carbon fibers and Sn particles, which can be applied to the surface of Na-β''-Al_2O_3. This modification enhances interface wettability and facilitates the uniform deposition of Na^+ [150]. A battery with $Na_3V_2(PO_4)_3$ as the cathode showed a capacity retention of 99.7% after 100 cycles at 5 C, indicating that the modified anode interface can adapt to high current density (Fig. 16b). Research has shown that, similar to $Li_7La_3Zr_2O_{12}$, eliminating hydroxyl groups and carbon contamination on the surface of Na-β''-Al_2O_3 through heat treatment is also crucial for improving the critical current density. Therefore, Battaglia *et al.* performed heat treatment on Na-β''-Al_2O_3 in an argon atmosphere and found that the interfacial resistance can be less than 10 Ω cm^2, and the current density can reach 12 mA/cm^2 (Fig. 17a) [151]. In addition, Liu *et al.* introduced a minor quantity of ionic liquid to the composite cathode, which can adhere to the surface of the SSE and maintain good interface contact with the SSE (Fig. 17b) [152]. The $Na_{0.66}Ni_{0.33}Mn_{0.67}O_2$/Na-$\beta''$-$Al_2O_3$/Na battery designed in this way has excellent rate performance and an exceptional cycle life, exceeding 10,000 cycles. Kim *et al.* even added liquid electrolyte to wet the interface at both sides, resulting battery showed significant advantages in capacity performance and cycling stability compared to liquid-state batteries (Fig. 17c) [145]. In addition, employing advanced techniques such as pulsed laser deposition for *in-situ* cathode deposition onto the electrolyte surface is a favorable approach to optimize the contact between the cathode and electrolyte [153].

Analogous to Na-β''-Al_2O_3, Nasicon-type SSEs also have excellent ionic conductivity, but the significant interface resistance arising from solid-solid contact in the all-solid-state SIBs greatly limits its performance [154]. Given their inherent brittleness, ceramic electrolytes often necessitate hot pressing to achieve optimal interface contact with electrode materials. Zhang *et al.* designed a $Na/Na_{3.3}Zr_{1.7}La_{0.3}Si_2PO_{12}/Na_3V_2(PO_4)_3$ battery [155]. Nonetheless, significant polarization was observed at room temperature, resulting in a modest reversible capacity of only 85 mAh/g during the initial cycle. Even when the cell was operated at 80 °C, the capacity dropped sharply after 40 cycles. The unsatisfactory electrochemical performance can be attributed to inadequate contact between the electrode material and SSEs. Despite the advantageous properties of high ionic conductivity and high elastic modulus in Nasicon,

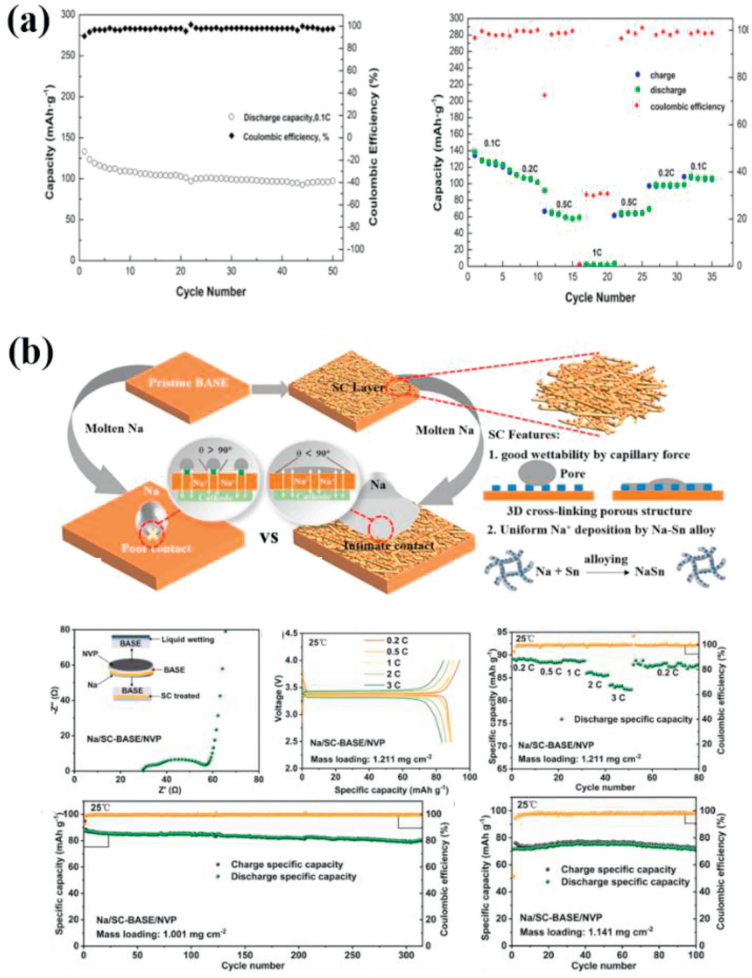

Fig. 16. (a) Cycling performance of the SIBs based on the Na-β''-Al_2O_3 thin film electrolyte. Reprinted with permission [148]. Copyright 2016, Elsevier. (b) Schematic illustration of $Na_3V_2(PO_4)_3$/SC-treated-β''-Al_2O_3/Na solid-state batteries and corresponding electrochemical performance. Reprinted with permission [150]. Copyright 2022, Elsevier.

the interface contact deteriorated over long-term cycling due to volume changes of the active material, making the cell unable to function properly even at high temperatures [156]. To improve interface compatibility, Zhang *et al.* also assembled two other types of cells, using a liquid electrolyte ($NaPF_6$/EC-DMC) and an ionic liquid (PP13FSI) as wetting agents, respectively (Fig. 18a) [155]. The incorporation of a liquid electrolyte partially enhanced the electrochemical performance. However, the specific capacity experienced a substantial decline after 250 cycles. This can be ascribed to the evaporation and/or decomposition of the liquid electrolyte. Additionally, the NVP/IL/SE/Na cell demonstrated the best cycling stability. This can be attributed to the enhanced interface contact between the electrode material and the solid electrolyte, forming a buffer layer. This buffer layer effectively mitigates interface resistance, minimizes cathode material volume change, and achieves excellent electrochemical performance. In addition to *in-situ* generation of intermediate layers by adding ionic liquids, some researchers directly add buffer layers between the cathode and electrolyte. Flexible solid materials are introduced between the cathode and electrolyte. Goodenough's team introduced plastic crystal electrolytes, which reduced interface impedance, increased cycle life, and allowed for high-rate performance, cycling more than 100 times at 5 C (Fig. 18b) [157]. Similarly, this interface layer is also introduced to the anode/electrolyte interface. Zhou and his colleagues added CPMEA between Na metal and Nasicon electrolyte (Fig. 19a) [158]. After 70 cycles at 0.2 C and 65 °C, a stable capacity of about 102 mAh/g was maintained, indicating that the Na/CPMEA/Nasicon interface has good stability and dendrite suppression ability. Ran *et al.* infused antioxidant polyacrylonitrile (PAN) and antioxidant polyethylene oxide (PEO) into a layered Nasicon framework comprising a compact core layer and a porous outer layer, and the polymer formed a tight and stable interface with the electrode, greatly reducing the interface resistance (Fig. 19b) [159]. The Na/SCE/NVPF battery demonstrates impressive cycling performance. After 460 cycles, the battery exhibits a capacity of 94 mAh/g with a capacity retention of 81%. In addition to soft organic interfacial layers, inorganic interfacial layers also find many applications. Yin *et al.* first introduced an AlF_3 coating between the Na metal and SSE, which can react with Na during the initial cycles to generate a Na^+ conductive buffer layer *in-situ*, increasing the interfacial area and suppressing Na dendrite growth by increasing the critical dendrite length (Fig. 20a) [160]. Wang *et al.* used a thermal decomposition method to construct an ultra-thin coating of SnS_2 between Nasicon and Na anode, and designed a $Na_3V_2(PO_4)_3$/$Na_3Zr_2Si_2PO_{12}$-SnS_2/Na battery, which exhibited remarkable rate performance (Fig. 20b) [161]. Furthermore, composite anodes are also an effective way to promote interfacial contact. Luo *et al.* added amorphous SiO_2 to the molten Na metal, which reduced surface tension and enabled close contact between the Na-SiO_2 composite material and Nasicon electrolyte, significantly reducing the interfacial resistance by 16 times and improving CCD performance by 5 times (Fig. 20c) [162].

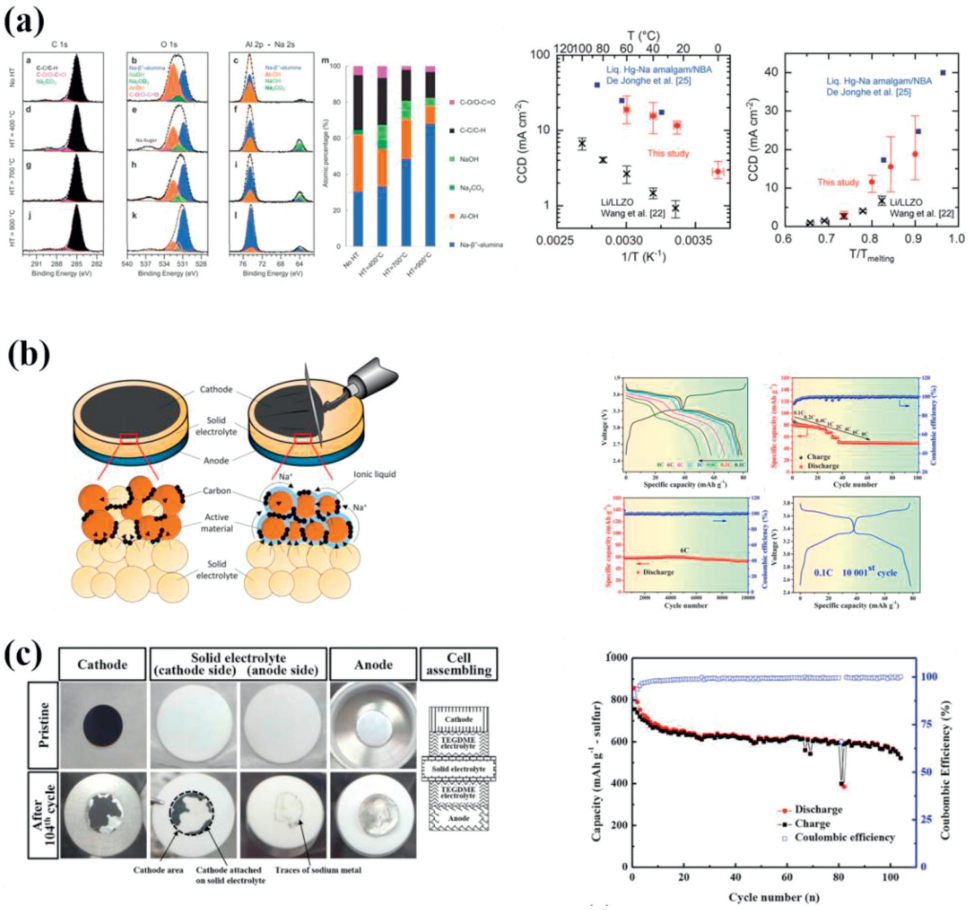

Fig. 17. (a) XPS spectra and surface composition analysis results of Na-β''-Al_2O_3 surfaces before and after heat treatment. Reprinted with permission [151]. Copyright 2019, Wiley Online Library. (b) Schematic illustration of $Na_{0.66}Ni_{0.33}Mn_{0.67}O_2/\beta''$-$Al_2O_3$/Na solid-state batteries with ionic liquid added in the cathode side and corresponding electrochemical performance. Reprinted with permission [152]. Copyright 2016, American Chemical Society. (c) Schematic illustration of solid-state batteries with liquid electrolyte added in the both sides of the interface between the cathode and anode electrodes and corresponding electrochemical performance. Reprinted with permission [145]. Copyright 2016, Elsevier.

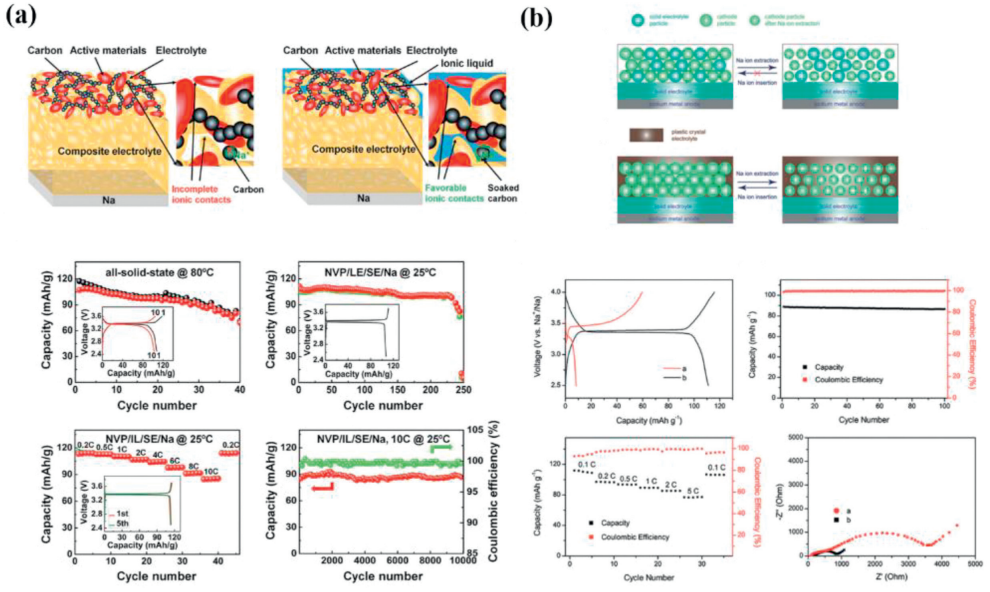

Fig. 18. (a) Schematic diagram of $Na_3V_2(PO_4)_3$/IL/$Na_{3.3}Zr_{1.7}La_{0.3}Si_2PO_{12}$/Na solid-state batteries and corresponding electrochemical performance. Reprinted with permission [155]. Copyright 2017, Wiley Online Library. (b) Schematic illustration of solid-state batteries with plastic-crystal electrolyte applied in the cathode and corresponding electrochemical performance. Reprinted with permission [157]. Copyright 2017, Wiley Online Library.

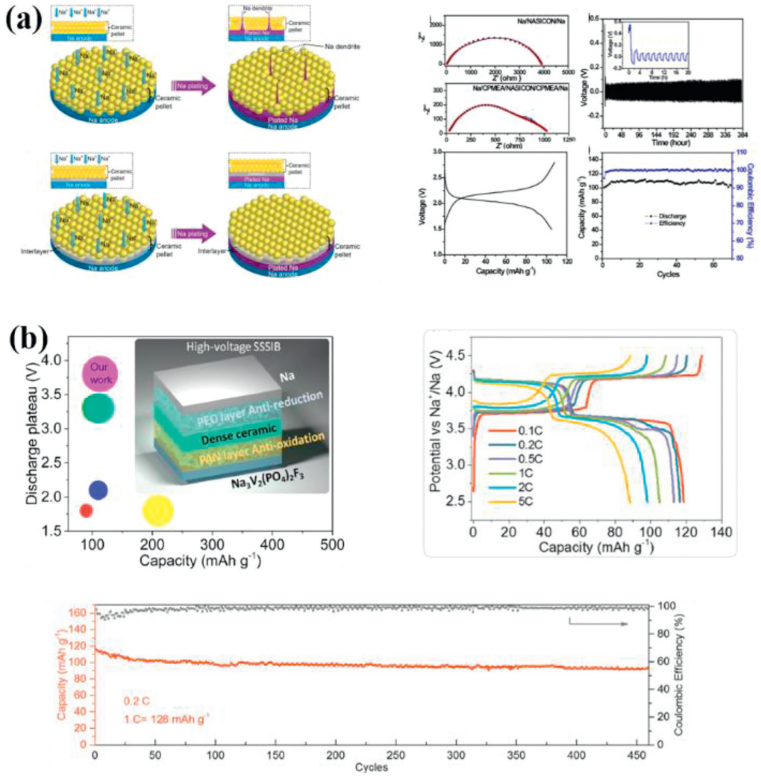

Fig. 19. (a) Schematic illustration of solid-state batteries with CMPEA added in the anode side and corresponding electrochemical performance. Reprinted with permission [158]. Copyright 2017, American Chemical Society. (b) Schematic illustration of solid-state sodium ion batteries with sandwich composite electrolyte and corresponding electrochemical performance. Reprinted with permission [159]. Copyright 2021, Elsevier.

Table 1
Summary of solid-state SIBs using oxide-based SSEs.

Battery type	Capacity in 1st cycle (mAh/g)	Cycling performance	Loading (mg/cm^2)	Refs.
$Na_{0.66}Ni_{0.33}Mn_{0.67}O_2/\beta''$-$Al_2O_3$/Na	60 (70 °C)	90%/10,000 cycles (6 C)	2	[152]
$Na_3V_2(PO_4)_3$/SC-treated-β''-Al_2O_3/Na	87.9 (25 °C)	91.1%/315 cycles (1 C)	1.001	[150]
$Na_3V_2(PO_4)_3$/Beta-Al_2O_3/UW-Na	95.4 (25 °C)	81.13%/800 cycles (0.5 C)	1	[163]
$K_2MnFe(CN)_6/Na_3Zr_2Si_2PO_{12}$/Na	117 (25 °C − 0 °C − 25 °C)	96%/900 cycles (1 C)	Not given	[164]
$Na_3V_2(PO_4)_3$/IL/$Na_{3.3}Zr_{1.7}La_{0.3}Si_2PO_{12}$/Na	90 (25 °C)	100%/10,000 cycles (10 C)	1.67	[155]
$Na_3V_2(PO_4)_3/AlF_3$-$Na_3Zr_2SiPO_{12}$/Na	111 (25 °C)	80.7%/100 cycles (1 C)	1.6	[160]
$Na_3V_2(PO_4)_3/Na_3Zr_2Si_2PO_{12}$-$SnS_2$/Na	104 (25 °C)	96.7%/100 cycles (1 C)	1	[161]
$Na_3V_2(PO_4)_3$/NZSP-0.1Ca/Na	96.7 (25 °C)	98.1%/450 cycles (1 C)	Not given	[165]
$NaCrO_2$/NZSP-0.2Mg/Na	110.9 (25 °C)	87%/1755 cycles (1 C)	1.5	[166]
$Na_3V_{1.5}Cr_{0.5}(PO_4)_3/Na_3Zr_2Si_2PO_{12}$−10%$Na_2B_4O_7$/Na	100 (25 °C)	88%/200 cycles (100 mA/g)	2–3	[167]
$NaCrO_2$/NZSP-0.2Cu/Na	83.4 (25 °C)	86.5%/660 cycles (5 C)	1.2–1.5	[168]
FeS_2/PDA-$Na_{3.4}Zr_{1.9}Zn_{0.1}Si_{2.2}P_{0.8}O_{12}$/Na	181.6 (60 °C)	73.3%/300 cycles (0.5 C)	1.0	[169]

Na-$Na_{15}Sn_4$ composite alloy is also frequently used to increase the diffusion coefficient of Na^+ in the anode.

In summary, both Na-β-β''-Al_2O_3 and Nasicon-type SSEs have similar strategies for optimizing the performance of batteries. Firstly, the grain boundary impedance of the oxide electrolyte is high, and high-temperature treatment is needed to improve material density and reduce grain boundary impedance. Secondly, common strategies to improve the electrode-electrolyte interface contact include thin film formation, liquid wetting or polymer addition, *in-situ* deposition, and porous structure design. Table 1 summarizes the performance of all-solid-state SIBs based on oxide Ni-ion SSEs [150,152,155,160,161,163–169].

5.2. Solid-state SIBs based on sulfide SSEs

Sulfide-based SSEs offer distinct advantages over oxide-based SSEs. They have higher ionic conductivity and are typically softer in texture, allowing for better contact with electrode materials through simple cold pressing and resulting in lower interfacial impedance. Therefore, the advancement of SIBs utilizing sulfide-based SSEs has attracted widespread attention. Nevertheless, several challenges remain to be addressed. Firstly, it pertains to the inherent stability of sulfide-based SSEs as numerous studies have highlighted their susceptibility to instability when exposed to air, leading to potential side reactions with water. Secondly, it is associated with ensuring the interface stability between sulfide-based SSEs and electrode materials [170–173].

Among the Various Na-ion SSEs investigated, the cubic Na_3PS_4 stands out for its exceptional Na-ion conductivity, surpassing 10^{-4} S/cm at room temperature [174]. Therefore, Wang *et al.* suggested the utilization of Na_3PS_4 as both a solid electrolyte and an active material, thereby establishing an inherent interface contact between the electrolyte and electrode [175]. The battery Na-Sn-C/Na_3PS_4/Na_3PS_4-Na_2S-C delivers a

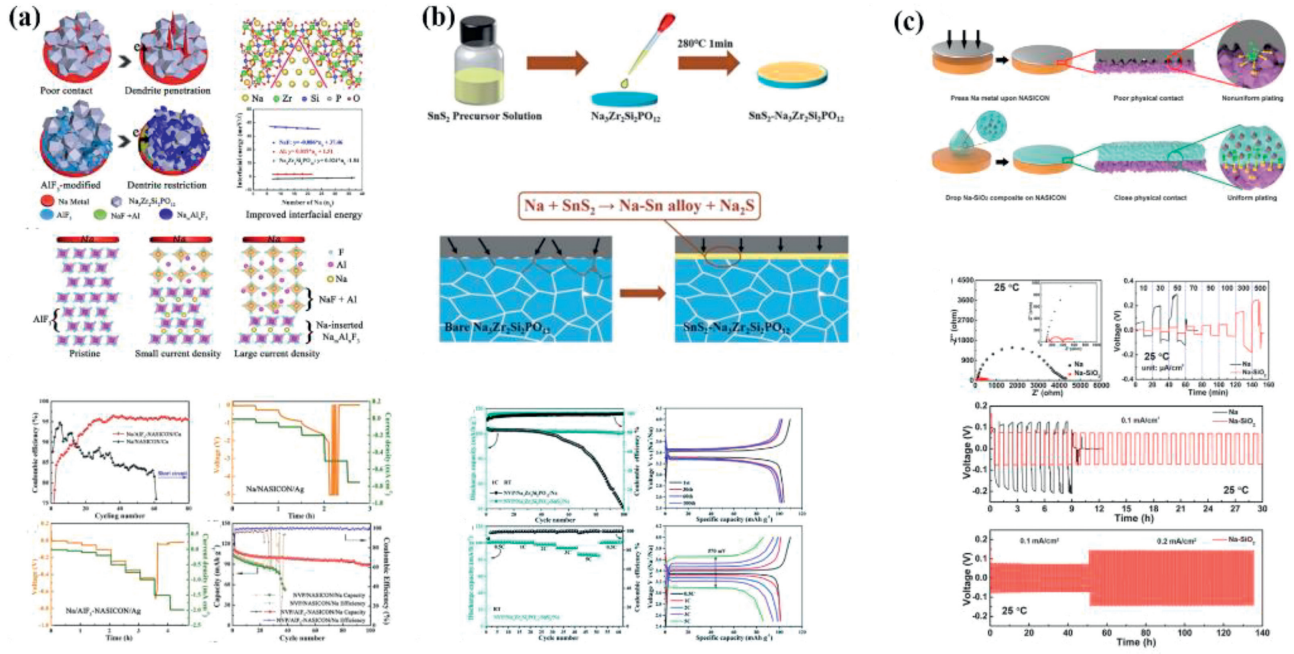

Fig. 20. (a) Schematic illustration of the AlF_3-modified Nasicon based cells and corresponding electrochemical performance. Reprinted with permission [160]. Copyright 2020, Elsevier. (b) Schematic illustration of the SnF_2-modified Nasicon based cells and corresponding electrochemical performance. Reprinted with permission [161]. Copyright 2021, Royal Society Chemistry. (c) Schematic illustration of the SiO_2-modified Nasicon based cells and corresponding electrochemical performance. Reprinted with permission [162]. Copyright 2020, American Chemical Society.

high reversible capacity of 869.2 mAh/g at 60 °C (Fig. 21a). In addition, Adams *et al.* proposed partially replacing P^{5+} with Sn^{4+}, leading to the highest ionic conductivity of the $Na_{3.1}Sn_{0.1}P_{0.9}S_4$ electrolyte composition (0.52 mS/cm) [176]. The $Na_{2+2\delta}Fe_{2-\delta}(SO_4)_3/Na_{3.1}Sn_{0.1}P_{0.9}S_4/Na_2Ti_3O_7$ battery was also prepared. After 100 cycles at 2 C at 80 °C, 82% of the initial capacity was retained (Fig. 21b). To address the air stability of the sulfide itself, Yao *et al.* produced a quaternary nano-solid electrolyte $Na_{10}SnSb_2S_{12}$ by a liquid-phase method, which exhibited excellent air stability [14]. The nano-sized electrolyte particles enhanced the interface contact between the electrolyte and electrode, resulting in a reduction in interface resistance. Therefore, the assembled $TiS_2/Na_{10}SnSb_2S_{12}$/Na SIBs exhibited good cycling performance (Fig. 21c). Furthermore, $Na_3P_{0.62}As_{0.38}S_4$ has good water stability and was used to prepare the $TiS_2/Na_3P_{0.62}As_{0.38}S_4$/Na-Sn solid-state battery [177]. The charge-discharge curve of the battery exhibited a significant irreversible capacity.

The narrow electrochemical window of sulfide electrolytes makes them prone to oxidation and reduction decomposition during battery cycling when matched with positive and anodes, leading to rapid performance degradation. Taking the well-established and widely studied Na_3PS_4 as an example, theoretical calculations show that its electrochemical window is about 1.55–2.25 V, which is poorly compatible with the electrochemical stability of high-voltage oxide cathodes, limiting its long cycle performance and practicality [178]. Therefore, Wu *et al.* constructed a battery, comprising a composite cathode composed of $NaCrO_2$ and NYZC, Na_3PS_4 electrolyte, and Na-Sn anode (Fig. 22a) [134]. At 20 °C and 0.1 C, the battery's first-cycle Coulombic efficiency increased sharply (from 71.9% to 97.6%). At 40 °C and 1 C conditions, it could cycle more than 1000 times with a capacity retention of 89.3%. The $NYZC_{0.74}$–$NaCrO_2$-VGCF composite cathode material exhibited stable electrochemical performance. However, in traditional cathode composite materials obtained by mechanical mixing, the electrolyte and cathode exhibit limited point-to-point contact, leading to reduce the utilization of the active material. Zhang *et al.* used a water-based solution to coat the surface of Se-doped SPAN active material with a layer of Na_3SbS_4, achieving close contact and uniform distribution between the electrolyte and electrode (Fig. 22b) [179]. The incorporation of the coating on the cathode resulted in a notable enhancement in Na^+ diffusion kinetics and a reduction in cathode diffusion impedance compared to the corresponding mixed cathode. In addition, the NSS coating also reduced the volume expansion effect of the cathode. The all-solid-state SIBs using the SeSPAN-Ar@NSS (1.23 mg/cm^2 area loading) cathode could provide good reversible capacity for over 150 cycles. Besides employing coating techniques to improving the cathode/electrolyte interface, finding cathode materials that are more compatible with sulfide solid electrolytes is also a direction for improving the cathode interface. Nagata *et al.* synthesized a series of amorphous $Na_{0.7}CoO_2$–Na_xMO_y (M = N, S, P, B, or C) composite electrode materials and found that this layered transition metal oxide and sodium-containing oxyacid salt composite amorphous material can effectively improve the discharge specific capacity of electrode material [180] . At the same time, the Yao's group also successively reported high-capacity quinone-based organic cathode materials $Na_4C_6O_6$ and pyrene-4,5,9,10-tetrone (PTO) (Fig. 22c) [183]. These materials exhibited good chemical and electrochemical compatibility with Na_3PS_4 electrolyte and resulted in very high specific capacity in all-solid-state SIBs, with outstanding stability, cycling stably for 400 and 500 cycles at 60 °C, respectively.

There are two primary challenges that need to be addressed in all-solid-state SIBs based on sulfide electrolytes with Na metal: interface compatibility and suppression of Na dendrite growth. Studies have shown that sulfide electrolytes such as Na_3PS_4 can decompose with metal Na to generate Na_2S and Na_3P, where the electronic conductivity of Na_3P is high, which can lead to continuous decomposition of the interface during cycling, increasing the total resistance. In recent times, numerous researchers have employed intermediate buffer layers, including ZrO_2, Sc_2O_3, and HfO_2, to enhance the interface compatibility between Na metal and sulfide electrolytes [182]. Li designed a phase-transition copolymer

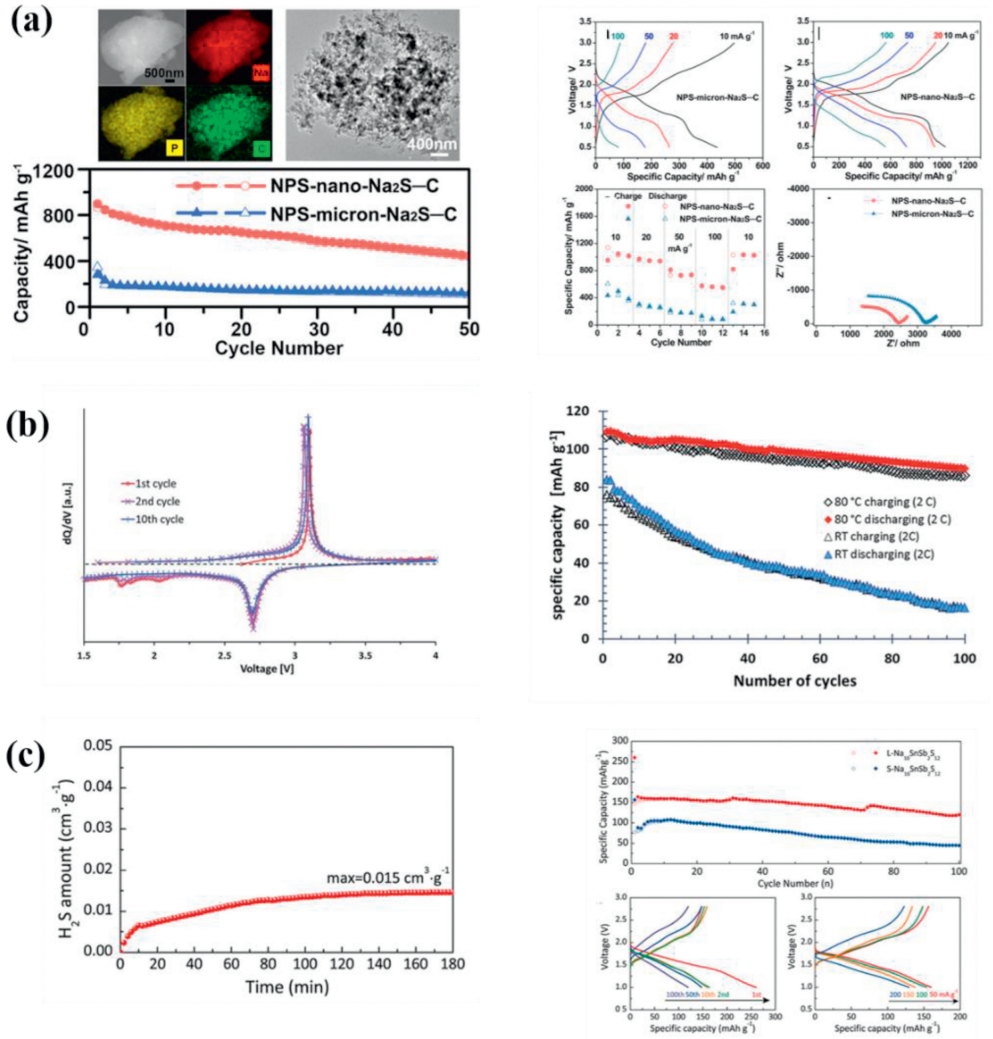

Fig. 21. (a) TEM images and corresponding elemental mappings of the NPS-nano-Na_2S-C nanocomposite cathode and electrochemical performance of the Na-Sn-C/Na_3PS_4/Na_3PS_4–Na_2S-C solid-state batteries. Reprinted with permission [175]. Copyright 2017, American Chemical Society. (b) Cycling performance of the $Na_{2+2\delta}Fe_{2-\delta}(SO_4)_3$/$Na_{3.1}Sn_{0.1}P_{0.9}S_4$/$Na_2Ti_3O_7$ solid-state batteries at different temperatures. Reprinted with permission [176]. Copyright 2017, Royal Society Chemistry. (c) The quantity of H_2S gas produced from $Na_{10}SnSb_2S_{12}$ exposed to humid air for different time durations and electrochemical performance of the TiS_2/$Na_{10}SnSb_2S_{12}$/Na solid-state batteries. Reprinted with permission [14]. Copyright 2021, Elsevier.

(PPP-NaTFSI) as the interlayer between the Na anode and Na_3SbS_4 (Fig. 23a) [183]. This work not only prevents the decomposition of sulfide but also facilitates the uniform deposition of sodium. Tian *et al.* discovered a hydrated phase $Na_3SbS_4{\cdot}8H_2O$ (Fig. 23b) [184]. The symmetric Na cell with untreated Na_3SbS_4 showed a continuously increasing voltage, while the cell with surface-hydrated Na_3SbS_4 exhibited only a small increase. The study showed that the hydrate reacted partially with metal Na upon contact, forming passive products NaH and Na_2O, which limited further decomposition of the Na_3SbS_4 solid electrolyte, reduced the growth of interface impedance during cycling, and improved interface stability with metal Na. Ionic liquids have low vapor pressure, good thermal stability, and good flow/wetting properties. Additionally, they also have good electrochemical compatibility with metal Na and Na alloy anodes. However, controlling the amount of ionic liquid additive is a key factor in improving battery performance. Therefore, Wang and colleagues presented a straightforward approach to optimize the utilization of ionic liquids (Fig. 23c) [185]. They used a PVDF membrane featuring sub-micron vertical channels to restrict the flow of ionic liquid, which enabled a uniform coating of BMTFSI with a thickness less than 500 nm on Na_3SbS_4 particles. The application of the coating offered several advantages. Firstly, it enhanced the physical contact between NSS particles, facilitating improved ion transport within the system. Secondly, it played a crucial role in effectively stabilizing the interface between NSS and metallic Na. The NVP/NSS/Na SIBs with an ionic coating structure exhibited excellent cycling and rate performance with over 400 cycles.

Surprisingly, Li *et al.* started from the electrolyte and proposed using $Na_4P_2S_{4.5}O_{2.5}$ oxysulfide as an additive to prepare a stable electrolyte-electrode interface by constructing a Na_3SbS_4 composite electrolyte (Fig. 24) [186]. For the first time, the behavior of different sub-lattices during cycling was revealed, and the migration of O ions was observed in the oxysulfide electrolyte. The Na//Na symmetrical cell showed high critical current density and long cycling stability of sodium plating/stripping, far exceeding that of the Na_3SbS_4 single-phase electrolyte. The assembled $Se_{0.8}S_{7.2}$@PAN/NaPSO+NSS/$Na_{15}Sn_4$ all-solid-state battery cycled 1000 times under room temperature and 0.3 C, demonstrating excellent electrochemical performance.

In general, in contrast to the rigid and fragile characteristics of oxide solid electrolytes, sulfide-based materials are relatively soft and can have good contact with electrode materials through simple cold pressing. Therefore, the strategy of using liquid wetting

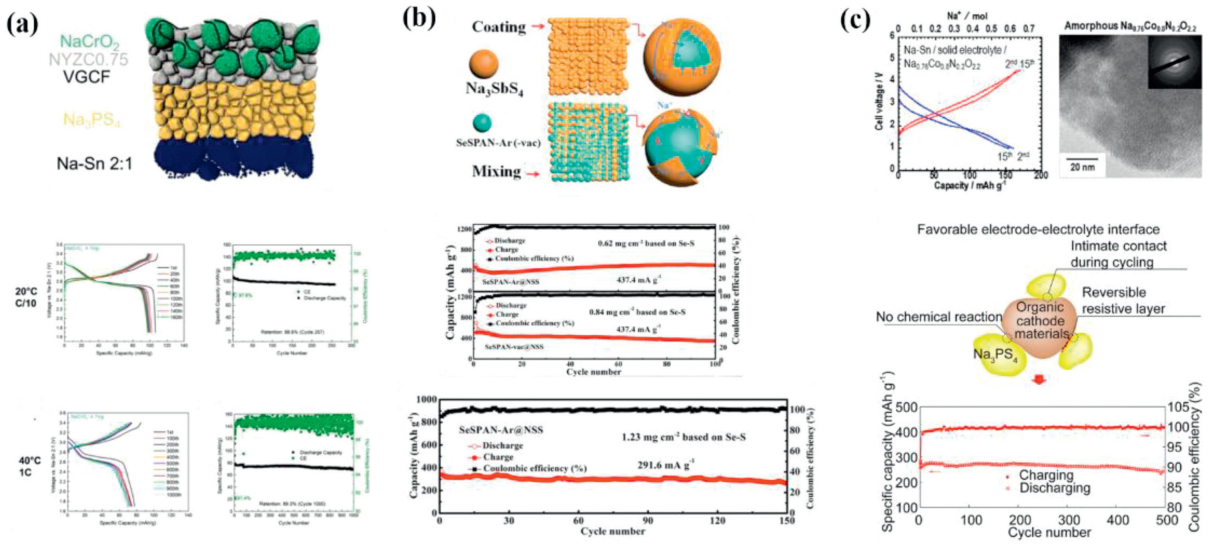

Fig. 22. (a) Schematic illustration of $NaCrO_2$+NYZC/Na_3PS_4/Na_2Sn solid-state batteries and corresponding electrochemical performance. Reprinted with permission [134]. Copyright 2021, Springer Nature. (b) Schematic illustration of SeSPAN-Ar@NSS/Na_3SbS_4/$Na_{15}Sn_4$ solid-state batteries and corresponding electrochemical performance. Reprinted with permission [179]. Copyright 2020, Elsevier. (c) Schematic illustration of SIBs with organic cathode and corresponding electrochemical performance. Reprinted with permission [180,181]. Copyright 2018, American Chemical Society. Copyright 2019, Cell Press.

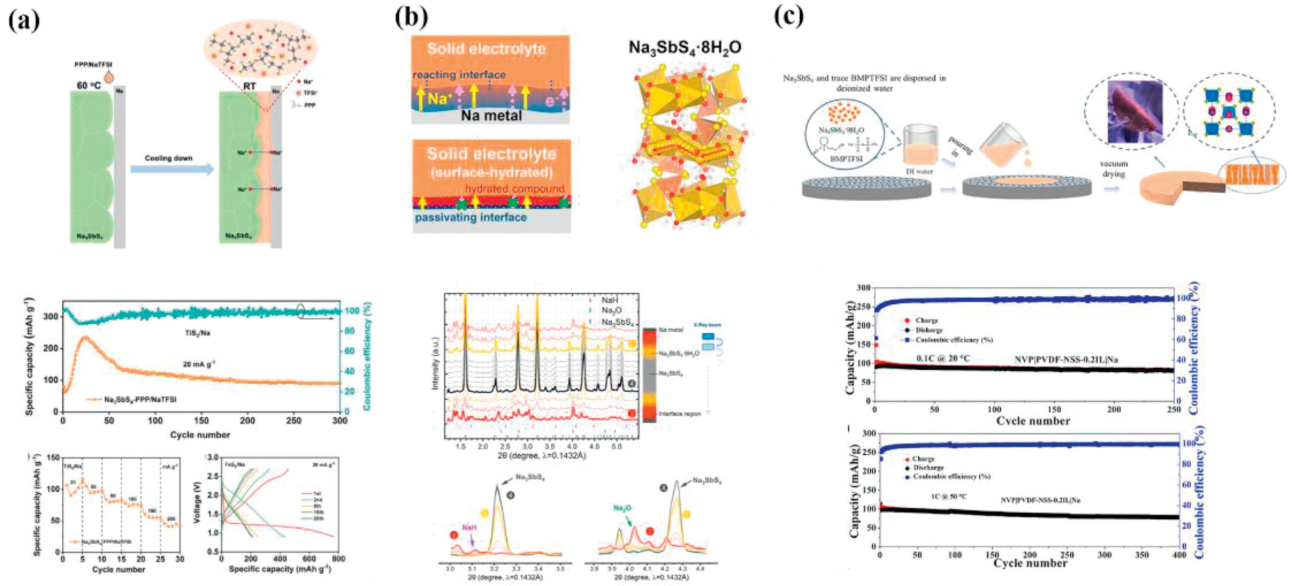

Fig. 23. (a) Schematic illustration of solid-state batteries with a phase-transition copolymer (PPP-NaTFSI) as the interlayer in the anode side and corresponding electrochemical performance. Reprinted with permission [183]. Copyright 2021, Wiley Online Library. (b) Schematic illustration of Na_3SbS_4 electrolyte with surface hydrate coating and corresponding SXRD profiles of Na/Na_3SbS_4/Na symmetric cell. Reprinted with permission [184]. Copyright 2019, Elsevier. (c) Schematic illustration of solid-state SIBs with PVDF membrane with sub-micron vertical channels and corresponding electrochemical performance. Reprinted with permission [185]. Copyright 2022, Elsevier.

agents at the interface is less commonly employed in sulfide-based all-solid-state SIBs. The main focus is on matching compatible positive and anode materials or introducing stable interfacial layers on both sides of the electrodes to prevent electrolyte oxidation and decomposition during battery cycling, which can lead to rapid performance degradation. Table 2 provides a summary of SIBs based on sulfide Na-ion SSEs [134,179,181,182,187–194].

5.3. Solid-state SIBs based on anti-perovskites SSEs

In recent years, researchers have started investigating Anti-perovskites Na-ion SSEs, which can exhibit extremely high ionic conductivity. However, these electrolytes exhibit high moisture susceptibility and have a tendency to absorb humidity [55,108]. Additionally, similar to oxide-type Na-ion SSEs, these electrolytes have relatively high grain boundary impedance, which limits their application in full cells. Braga *et al.* utilized precursor materials similar to Na_3OCl and conducted a series of heat treatments after mixing the raw materials in a deionized water environment. This process resulted in the formation of an amorphous glassy electrolyte, $Na_{3-x}H_xOCl$ ($0 < x < 1$) [195]. Na/ferrocene cells assembled with $Na_{3-x}H_xOCl$ as the solid electrolyte demonstrate good cycling stability at room temperature (Fig. 25a). Unlike traditional oxide SSEs, perovskite-type Na-ion SSEs can be synthesized at lower temperatures, making them easier to process. They also exhibit higher ionic conductivity. If the solid-solid interface contact issue is properly addressed, this material holds great potential for application in all-solid-state SIBs. Fan *et al.* synthesized

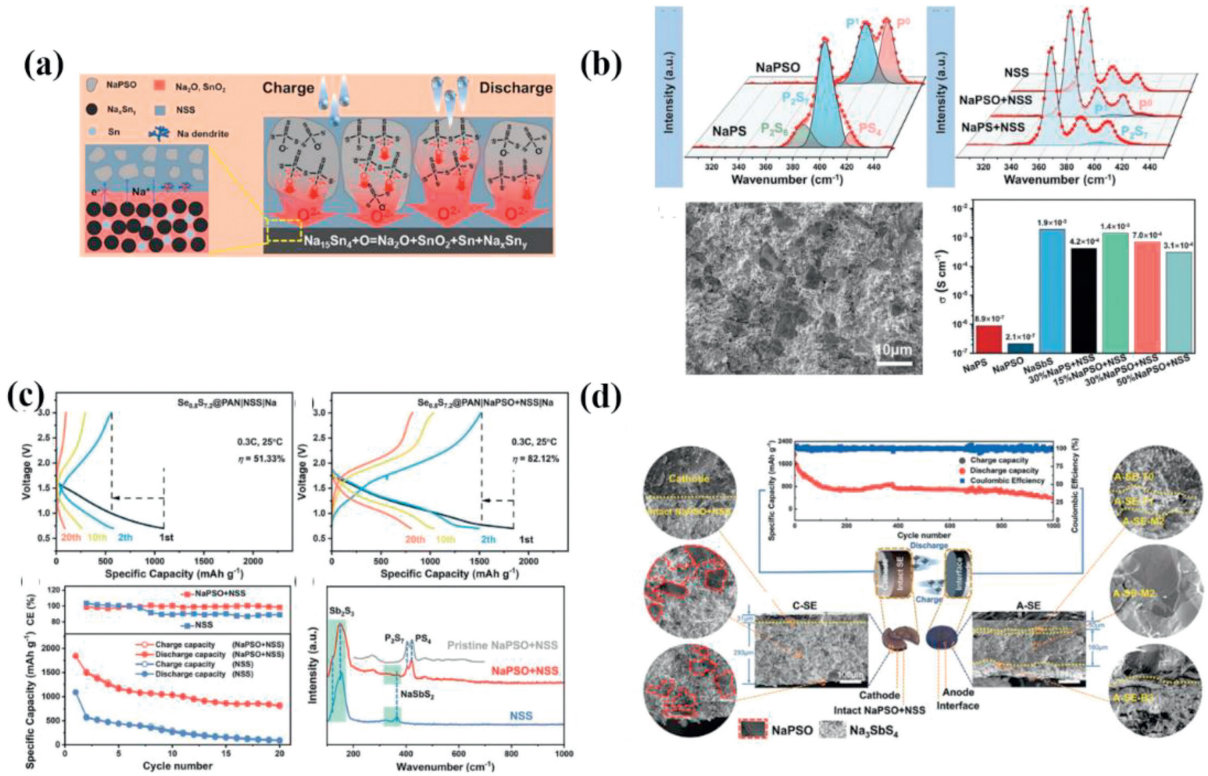

Fig. 24. (a) Mechanism schematic illustration of the $Se_{0.8}S_{7.2}$@PAN/NaPSO+NSS/$Na_{15}Sn_4$ solid-state batteries. (b) Raman spectra, SEM image and Ionic conductivity of NaPSO+NSS. (c) electrochemical performance of the $Se_{0.8}S_{7.2}$@PAN/NaPSO+NSS/$Na_{15}Sn_4$ solid-state batteries. (d) Cross-sectional SEM images and EDS mapping for the $Se_{0.8}S_{7.2}$@PAN/NaPSO+NSS/$Na_{15}Sn_4$ and corresponding electrochemical performance. Reprinted with permission [186]. Copyright 2022, Wiley Online Library.

Table 2
Summary of solid-state SIBs using sulfide-based SSEs.

Battery type	Loading (mg/cm^2)	Theoretical and 1st discharge capacity (mAh/g)	Cycle performance (%)	Refs.
$Se_{0.8}S_{7.2}$@PAN|$Na_4P_2S_{4.5}O_{2.5}$+Na_3SbS_4|$Na_{15}Sn_4$	2.6	1675, ~1639 (0.3 C)	1000, 22.5 (25 °C)	[186]
$Fe_{1-x}S$@$Na_{2.9}PS_{3.95}Se_{0.05}$|$Na_{2.9}PS_{3.95}Se_{0.05}$|Na	2.0	894, ~680 (100 mA/g)	100, 75.45 (25 °C)	[187]
FeS_2|Na_3PS_4|Na	2.0	894, ~350 (60 mA/g)	100, 80 (25 °C)	[188]
SE-coated Mo_6S_8|Na_3PS_4|Na-Sn-C	5.0	123. ~80 (60 mA/g)	500, ~69 (60 °C)	[189]
$Na_4C_6O_6$|Na_3PS_4|$Na_{15}Sn_4$	3.0	184, ~130 (0.2 C)	400, ~68 (60 °C)	[190]
PTO–Na_3PS_4–C|Na_3PS_4|$Na_{15}Sn_4$	5.0	409, ~265 (0.3 C)	500, ~89 (60 °C)	[181]
$Se_{0.05}S_{0.95}$@pPAN|Na_3PS_4|Na_3Sn	4.0	1500, ~880 (0.3 A/g)	50, ~42 (25 °C)	[191]
SeS_2–Na_3SbS_4–C|Na_3SbS_4|$Na_{15}Sn_4$	5	1342, ~450 (0.3 C)	60, 325 (25 °C)	[192]
SeSPAN-Ar@NSS||Na_3SbS_4||$Na_{15}Sn_4$	1.23	1675, ~509 (291.6 mA/g)	100, 98.9 (25 °C)	[179]
$NaCrO_2$+$NaAlCl_4$|NaPS|Na_3Sn	22.6	120, 112 (1 C)	500, 82 (60 °C)	[193]
$NaCrO_2$+NYZC|NaPS|Na_2Sn	12	120, 78 (1 C)	1000, 89.3 (40 °C)	[134]
S-(KB)-$Na_3PS_{3.85}O_{0.15}$|$Na_3PS_{3.85}O_{0.15}$|$Na_3PS_{3.4}O_{0.6}$|Na	~1	1675, 1280 (0.1 mA/cm^2)	40, 80 (60 °C)	[194]

an innovative anti-perovskite SSEs, $Na_{2.98}Mg_{0.01}SO_4F_{0.95}Cl_{0.05}$, using low-cost precursors through a solid-state reaction at 500 °C (Fig. 25b) [54]. The incorporation of Mg^{2+} and Cl^- led to a three-order-of-magnitude increase in ionic conductivity, reaching approximately 10^{-4} S/cm at 60 °C. Based on this electrolyte, a $Fe[Fe(CN)_6]_3$/$Na_{2.98}Mg_{0.01}SO_4F_{0.95}Cl_{0.05}$/Na-Sn solid-state battery was assembled, demonstrating reversible operation. The battery exhibited an initial discharge capacity of 91.0 mAh/g, which was followed by a sustained reversible capacity of 77.0 mAh/g. Jiang *et al.* investigated a vacancy-deficient cluster-ion based anti-perovskite solid-state electrolyte called $Na_2BH_4NH_2$ (Fig. 25c) [196]. A NaSn|$Na_2BH_4NH_2$|NaSn symmetric cell was cycled for 500 h at a current density of 0.1 mA/cm^2. Furthermore, the compatibility of $Na_2BH_4NH_2$ electrolyte with electrode materials was demonstrated using TiS_2 cathode, indicating good compatibility between $Na_2BH_4NH_2$ and electrode materials.

5.4. Solid-solid SIBs based on complex hydrides SSEs

Orimo's group was among the first to develop sodium-based complex hydrides SSEs and investigate their electrochemical performance in solid-state batteries [63]. These complex hydrides typically exhibit a characteristic first-order phase transition at a certain temperature, with a several-orders-of-magnitude increase in conductivity from the low-temperature phase to the high-temperature phase [197]. However, the relatively high phase transition temperature has limited their application in all-solid-state SIBs. Over the past few years many researchers have successfully lowered the phase transition temperature of some materials to room temperature or even eliminated the phase transition through chemical modifications, size control, partial anion substitution, or mixing different anions [198–201]. These advancements have greatly facilitated their application in solid-state bat-

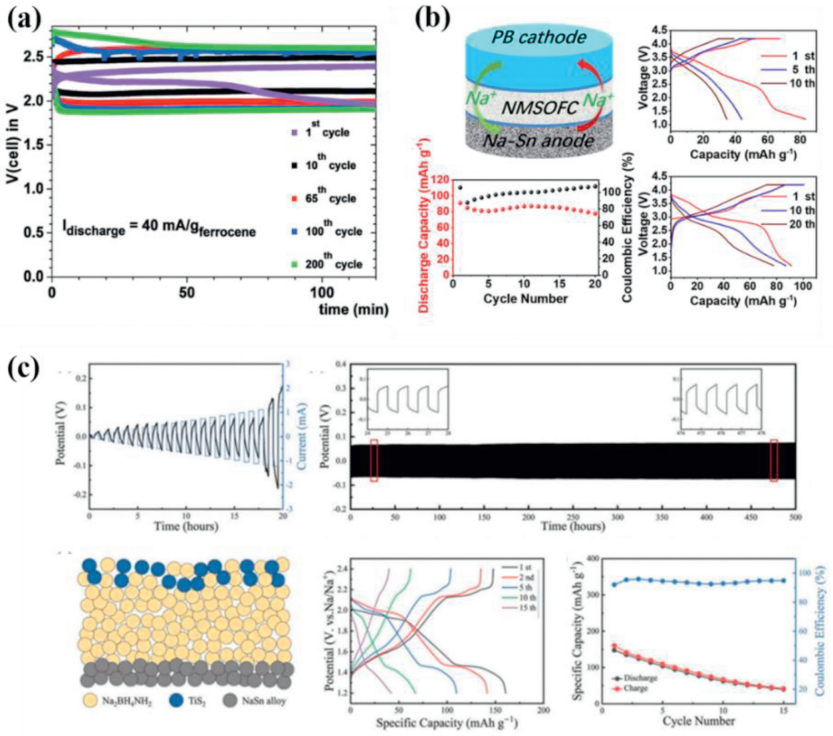

Fig. 25. (a) Cycling performance of the Na/ferrocene cells assembled with $Na_{3-x}H_xOCl$. Reprinted with permission [195]. Copyright 2017, Royal Society Chemistry. (b) Schematic illustration of $Fe[Fe(CN)_6]_3/Na_{2.98}Mg_{0.01}SO_4F_{0.95}Cl_{0.05}$/Na-Sn and corresponding electrochemical performance. Reprinted with permission [54]. Copyright 2020, Elsevier. (c) Electrochemical performance of NaSn|$Na_2BH_4NH_2$|NaSn symmetric cell and TiS_2|$Na_2BH_4NH_2$|NaSn solid-state batteries. Reprinted with permission [196]. Copyright 2023, Wiley Online Library.

teries. Although the optimized sodium ion complex hydrides electrolytes have significantly improved conductivity, the reported all-solid-state SIBs using complex hydrides electrolytes are still limited due to factors such as large interfacial resistance and poor cycling stability. So far, most all-solid-state SIBs using complex hydrides electrolytes have employed TiS_2 or $NaCrO_2$ cathodes with a voltage range of around 3 V. In recent years, some researchers have utilized mixed borohydrides as solid electrolytes in all-solid-state SIBs. Yoshida *et al.* obtained pseudo-binary complex hydrides as Na-ion SSEs by mechanically ball-milling pure $Na_2B_{10}H_{10}$ and $Na_2B_{12}H_{12}$ [202]. The ion conductivity of the mixture showed a direct correlation with the fraction of the body-centered cubic phase. It reached the maximum value when the molar ratio was 1:3. The initial specific discharge capacity of the cell assembled with Na metal anode and TiS_2 cathode is close to the theoretical capacity of TiS_2 (239 mAh/g). Duchêne *et al.* developed a $NaCrO_2$|$Na_2(B_{12}H_{12})_{0.5}(B_{10}H_{10})_{0.5}$|Na battery [203]. By impregnating the electrolyte solution onto the cathode particles to improve the electrode-electrolyte contact, a stable solid-solid interface was established between the electrolyte and the cathode, enhancing the battery performance (Fig. 26a). This resulted in reversible and stable cycling. After 20 cycles at 0.05 C, the capacity retention exceeded 90%, and after 250 cycles at 0.2 C, the capacity retention reached 85%. The Duchêne research group also infiltrated the soluble-processed complex hydrides $Na_4(B_{12}H_{12})(B_{10}H_{10})$ into a porous electrode made through slurry casting [204]. They reported that an all-solid-state SIBs with a $NaCrO_2$ electrode infiltrated with $Na_4(B_{12}H_{12})(B_{10}H_{10})$ maintained 95.6% of its initial capacity after 100 cycles at 0.5 C (Fig. 26b).

Further investigations have focused on a subgroup of complex hydrides, borohydrides, and their C-derived compounds known as carba–closo-borates, which exhibit excellent conductivity values even at room temperature. Murgia *et al.* recorded a fast Na^+ conductor, $Na_4(CB_{11}H_{12})_2(B_{12}H_{12})$ [205]. Integrating this electrolyte into a Na/$NaCrO_2$ battery demonstrated excellent electrochemical performance (Fig. 27a). The specific capacity of the battery was approximately 100 mAh/g at an output current density of 24 mA/g. *In-situ* EIS testing during cycling revealed a stable Na-Na symmetric cell, with the conductor enabling stable Na plating/stripping for over 500 h, exhibiting limited polarization and low interfacial resistance. Brighi *et al.* synthesized a novel compound, $Na_{2-x}(CB_{11}H_{12})_x(B_{12}H_{12})_{1-x}$ (Fig. 27b) [206]. Symmetric cells with Na-Sn alloy electrodes exhibited reversible Na^+ shuttling and limited polarization over a working period exceeding 700 h, demonstrating their electrochemical stability. In addition, He and colleagues proposed an innovative Na^+ conductor $Na_3NH_2B_{12}H_{12}$ (Fig. 27c) [207]. It has an impressive electrochemical window of 10 V *vs.* Na^+/Na. By utilizing this electrolyte, an all-solid-state SIBs was constructed with a TiS_2 cathode and Na foil anode. Operating at 80 °C and 0.1 C, the battery demonstrated over 200 reversible cycles with a capacity retention rate exceeding 50%.

The electrochemical window of most complex hydrides is narrow, with the electrochemical stability primarily limited to 4 V. This incompatibility with 4 V cathode materials results in lower energy density. To address this issue, Remhof's research group showcased the effectiveness of a hydroborate-based electrolyte, $Na_4(CB_{11}H_{12})_2(B_{12}H_{12})$, which comprises two distinct cage-like anions with varying oxidation stability. This electrolyte demonstrated successful interface passivation with high-voltage cathodes operating at 4 V, effectively mitigating impedance growth during cycling [208]. They achieved the first demonstration of a 4 V-level complex hydrides electrolyte-based all-solid-state SIBs. The battery employed $Na_3(VOPO_4)_2F$ as the cathode and Na metal as the anode, without any artificial coating or protection. The configuration of the battery was $Na_3(VOPO_4)_2F/Na_4(CB_{11}H_{12})_2(B_{12}H_{12})$/Na. When cycled to 4.15 V *vs.* Na^+/Na at 0.1 C, the battery exhibited a discharge capacity of 104 mAh/g, and at 0.2 C, the capacity was 99 mAh/g. After 800 cycles at room tempera-

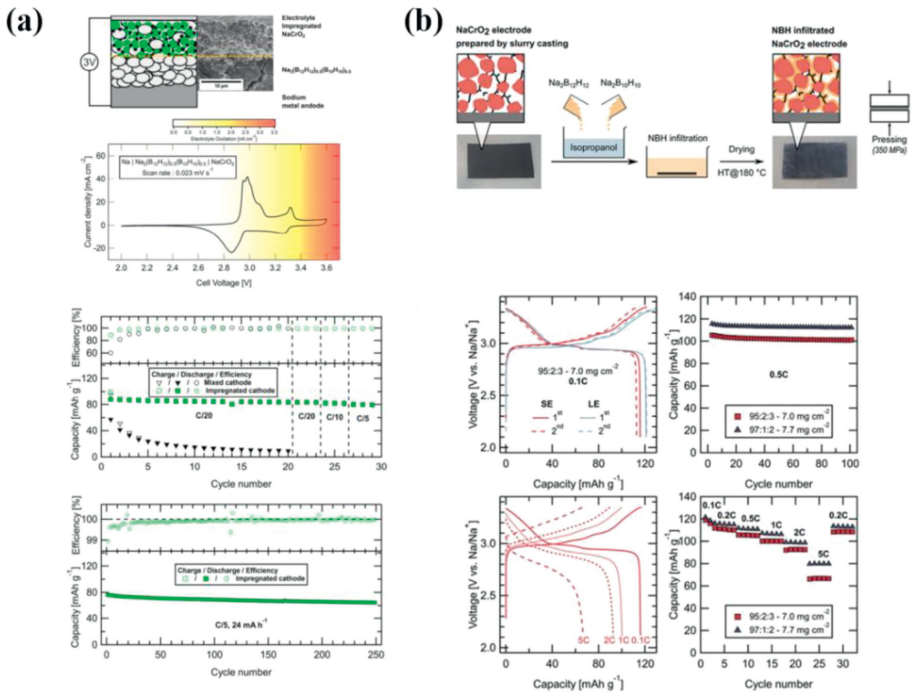

Fig. 26. (a) Schematic illustration of $NaCrO_2|Na_2(B_{12}H_{12})_{0.5}(B_{10}H_{10})_{0.5}|Na$ solid-state batteries and corresponding electrochemical performance. Reprinted with permission [203]. Copyright 2013, Royal Society Chemistry. (b) Schematic illustration of solid-state batteries with a $NaCrO_2$ electrode infiltrated with $Na_4(B_{12}H_{12})(B_{10}H_{10})$ and corresponding electrochemical performance. Reprinted with permission [204]. Copyright 2020, Elsevier.

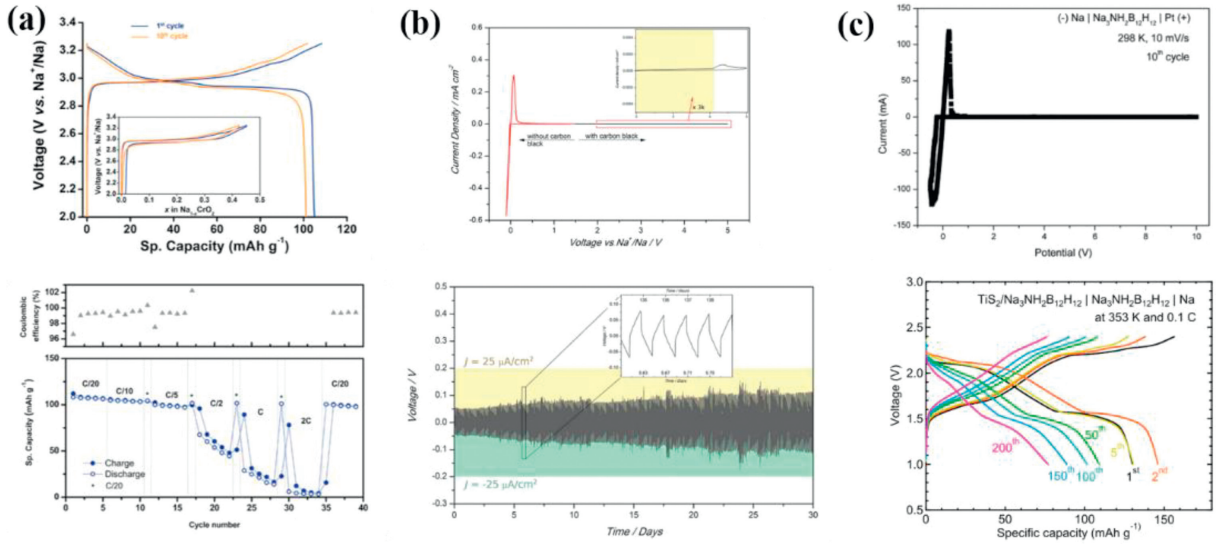

Fig. 27. (a) Electrochemical performance of $NaCrO_2/Na_4(CB_{11}H_{12})_2(B_{12}H_{12})/Na$ solid-state batteries. Reprinted with permission [205]. Copyright 2019, Elsevier. (b) Electrochemical performance of $NaSn/Na_{4/3}(CB_{11}H_{12})_{2/3}(B_{12}H_{12})_{1/3}/NaSn$ symmetric cell. Reprinted with permission [206]. Copyright 2018, Elsevier. (c) CV test results for $Na/Na_3NH_2B_{12}H_{12}/Pt$ and electrochemical performance of $TiS_2/Na_3NH_2B_{12}H_{12}/Na$ solid-state batteries. Reprinted with permission [207]. Copyright 2018, Elsevier.

ture, the capacity retention rates were 78% and 76%, respectively (Fig. 28a). Furthermore, Guo and collaborators achieved, for the first time, an electrochemical stability window using the novel complex hydrides $Na_3B_{24}H_{23}$ (6.7 V *vs.* Na^+/Na) as the electrolyte [209]. A high-voltage all-solid-state sodium battery, $Na[Ni_{1/3}Fe_{1/3}Mn_{1/3}]O_2/Na_3B_{24}H_{23}–5Na_2B_{12}H_{12}/Na$, was assembled using $Na_3B_{24}H_{23}–5Na_2B_{12}H_{12}$ in conjunction with a 4 V-level cathode. After 100 cycles at 60 °C and 0.1 C, the capacity retention rate reached 84% (Fig. 28b). This discovery provides an opportunity for the development of novel complex hydrides electrolyte-based all-solid-state SIBs with high voltage and high energy density.

In general, complex hydrides electrolytes have shown superior compatibility with metallic Na, high chemical/stability, good mechanical properties, low weight density, excellent solution processability, and low toxicity. Particularly, their high deformability and high solubility are advantageous for processing into solid-state batteries. However, the complex synthesis process and electrochemical instability limit their application in solid-state batteries. So far, only a few complex hydride SSEs have been developed and applied in all-solid-state SIBs. Table 3 summarizes the solid-state batteries based on complex hydrides Na-ion electrolytes [202,203,205,207–211]. Furthermore, although complex hydrides have a notable impact on stabilizing the deposition/stripping of sodium, the properties of their electrochemical decomposition products are still unclear and require further investigation.

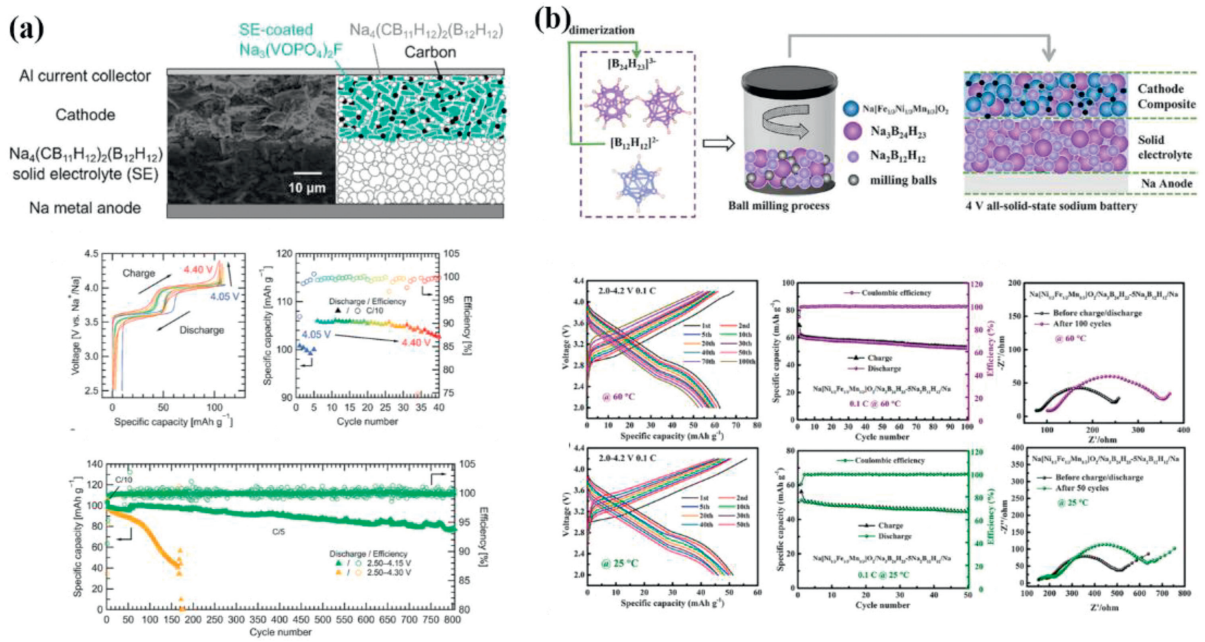

Fig. 28. (a) Schematic illustration of $Na_3(VOPO_4)_2F/Na_4(CB_{11}H_{12})_2(B_{12}H_{12})$/Na solid-state batteries and corresponding electrochemical performance. Reprinted with permission [208]. Copyright 2020, Royal Society Chemistry. (b) Schematic illustration of $Na[Ni_{1/3}Fe_{1/3}Mn_{1/3}]O_2/Na_3B_{24}H_{23}–5Na_2B_{12}H_{12}$/Na solid-state sodium batteries and corresponding electrochemical performance. Reprinted with permission [209]. Copyright 2023, Elsevier.

Table 3
Summary of solid-state SIBs using complex hydrides SSEs.

Battery type	Capacity in 1st cycle (mAh/g)	Cycling performance	Loading	Refs.
$TiS_2/Na_2B_{10}H_{10}–3Na_2B_{12}H_{12}$/Na	254 (30 °C)	91%/11 cycles (0.02 C)	Not given	[202]
$NaCrO_2/Na_2(B_{12}H_{12})_{0.5}(B_{10}H_{10})_{0.5}$/Na	85 (60 °C)	90%/20 cycles (0.05 C)	2 mg (1.77 mg/cm^2)	[203]
$NaCrO_2/Na_2(B_{12}H_{12})_{0.5}(B_{12}H_{12})_{0.5}$/Na	80 (60 °C)	85%/250 cycles (0.2 C)	2 mg (1.77 mg/cm^2)	[203]
$TiS_2/Na_3NH_2B_{12}H_{12}$/Na	146 (80 °C)	53%/200 cycles (0.1 C)	0.6 mg (1.2 mg/cm^2)	[207]
$NaCrO_2/Na_4(B_{12}H_{12})(B_{10}H_{10})$/Na	118 (30 °C)	95.6%/100 cycles (0.5 C)	7.7 mg/cm^2	[210]
$NaCrO_2/Na_4(CB_{11}H_{12})_2(B_{12}H_{12})$/Na	108.6 (25 °C)	94%/10 cycles (6 mA/g)	2 mg (7.08 mg/cm^2)	[205]
$Na_{0.7}Mn_{0.5}Ni_{0.2}Co_{0.3}O_2/Na(CB_9H_{10})_{0.7}(CB_{11}H_{12})_{0.3}$/hard carbon	240 (25 °C)	97%/100 cycles (0.115 mA/cm^2)	5.8 mg/cm^2	[211]
$Na[Ni_{1/3}Fe_{1/3}Mn_{1/3}]O_2/Na_3B_{24}H_{23}–5Na_2B_{12}H_{12}$/Na	68.9 (60 °C)	84%/100 cycles (0.1 C)	2 mg	[209]
$Na_3(VOPO_4)_2F/Na_4(CB_{11}H_{12})_2(B_{12}H_{12})$/Na	99 (25 °C)	76%/800 cycles (0.2 C)	2 mg (1.2 mg/cm^2)	[208]

5.5. Solid-state SIBs based on halide SSEs

In recent years, lithium halide superionic conductors have been widely studied. Generally, lithium halides can maintain oxidation limits exceeding 4 V, demonstrating good (electro)chemical stability with active materials such as $LiCoO_2$ and NCM811. Although sodium halides are not as good as lithium halides in terms of high-pressure stability and ion conductivity, they can still be used as ion conductor additives in high-pressure oxide-based cathodes instead of sulfide electrolytes. For example, Na_2ZrCl_6, $Na_{3-x}Y_{1-x}Zr_xCl_6$, and $NaAlCl_4$ (synthesized by ball milling/mechanochemical methods) have shown good compatibility with $NaCrO_2$. Li *et al.* found that $NaYbZrCl_{0.75}$ additive exhibits good compatibility with $NaCrO_2$, inducing a positive effect on the volume change during cathode cycling. It induces the formation of a special core-shell structure on the surface of $NaCrO_2$ grains, with uniform $NaYbZrCl_{0.75}$ encapsulation, promoting uniform ion transport and alleviating (electro)chemical mechanical stress. The all solid-state SIBs with $NaYbZrCl_{0.75}$ additive exhibits good cycling stability, maintaining a capacity retention of 74.1% after 1000 cycles at 25 ± 3 °C and 83.0% after 1900 cycles at 60 °C (Fig. 29a) [135]. Fu *et al.* developed a novel class of halide heterostructure electrolytes with good deformability and high-pressure stability, enabling stable cathode/electrolyte interfaces with $Na_{0.85}Mn_{0.5}Ni_{0.4}Fe_{0.1}O_2$ cathode through simple cold pressing, achieving a capacity retention of 91.0% after 100 cycles at 0.2 C in all solid-state SIBs [212]. In addition, Hu *et al.* successfully combined a Na-ion halide electrolyte ($NaTaCl_6$) with a poly-anion-type $Na_3V_2(PO_4)_3$ cathode for the first time, demonstrating stable long-term cycling performance after 4000/600/1500 cycles at 3/1/0.5 C rates, with capacity retentions of 81%/95%/98%, respectively. The comprehensive performance of the reported all solid-state SIBs surpasses all previously reported results (Fig. 29b) [138].

After optimization, Na-ion halides electrolyte generally exhibit good ion conductivity, wide electrochemical oxidation windows, and a certain degree of toughness, making them excellent positive electrode ion conductor additives for use in all-solid-state batteries. In conclusion, halide electrolytes hold promising prospects in the field of batteries, especially suitable for high voltage and high-performance requirements, thus offering more efficient and sustainable energy storage solutions for future renewable energy applications.

6. Advanced characterizations for solid-state sodium batteries

Although many researchers have made significant efforts to address interface issues in electrode/electrolyte interfaces, there are still many unanswered questions, such as the exact composition and structure of the interfaces, their evolution processes, their correlation with battery performance, and the formation mechanisms.

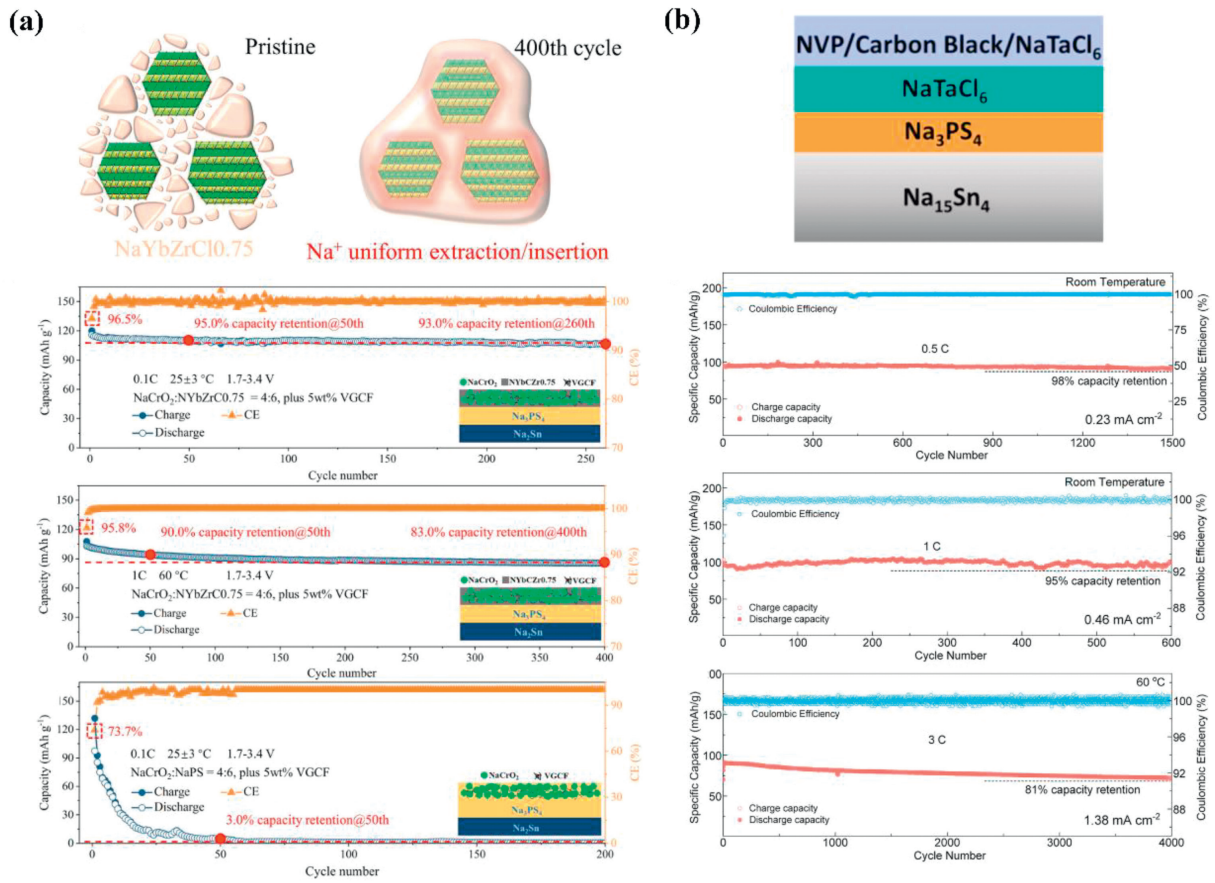

Fig. 29. (a) Schematic diagram illustrating the structural changes in the composite cathode of $NaCrO_2$-$NYbZrCl_{0.75}$/Na_3PS_4/Na_2Sn solid-state batteries and corresponding electrochemical performance. Reprinted with permission [135]. Copyright 2023, Elsevier. (b) Schematic illustration of NVP/$NaTaCl_6$/Na_3PS_4/$Na_{15}Sn_4$ solid-state sodium batteries and corresponding electrochemical performance [138]. Copyright 2023, Cell Press.

To convincingly answer these questions, more advanced characterization techniques need to be developed to uncover clues. Currently, some literature has used certain characterization techniques to reveal the structural features and functional mechanisms of the constructed electrode/electrolyte interfaces accurately and intuitively. Furthermore, different characterization techniques can be classified as *in-situ* or *ex-situ*. *In-situ* characterization, compared to *ex-situ* characterization, directly reveals the internal electrochemical processes of redox reactions, allowing real-time monitoring of the evolution of interface composition and structure. While *in-situ* characterization provides direct evidence of the internal redox reactions in batteries, such tests are often operationally challenging and have specific requirements for the testing equipment. Therefore, the available types of techniques for *in-situ* characterization are still quite limited.

Similar to lithium, dendritic growth of sodium also occurs in the form of branching, causing short circuits in sodium metal batteries. Considerable investigation has been undertaken to explore the mechanisms governing the growth and deposition of lithium dendrites. However, there is limited research on sodium dendrite growth and sodium deposition. The dynamics of sodium dendrite deposition/stripping are still not well understood, which hampers the development of strategies for uniform sodium deposition and stripping. Therefore, real-time observation of metal sodium deposition and stripping is crucial to understanding their growth mechanisms and inhibiting the formation of sodium dendrites. Huang *et al.* conducted real-time observation studies on sodium dendrite growth and stripping in a carbon dioxide atmosphere using advanced aberration-corrected environmental transmission electron microscopy (ETEM) [213]. It is worth noting that the deposition rate can be adjusted by controlling the applied voltage. Therefore, the morphology of deposited sodium can be controlled by adjusting the applied voltage, which may provide important clues for mitigating dendritic growth in all-solid-state SIBs. In a recent investigation, Huang *et al.* performed *in-situ* optical microscopy (OM) examinations to observe the growth of Na dendrites in a symmetric cell Na/β''-Al_2O_3/Na [214]. Complementing this analysis, they employed *in-situ* SEM to examine the dynamic interplay between Na deposition and the propagation of cracks. The outcomes of their research demonstrated that crack formation preceded the deposition of Na, with subsequent Na deposition inducing the generation of additional cracks. Notably, Na deposition persisted alongside crack propagation until a short circuit event was triggered. This study substantially contributes to our comprehension of the failure mechanisms inherent in all-solid-state SIBs employing Na-β''-Al_2O_3 SSEs.

So far, there has been relatively limited research on the mechanical properties related to sodium dendrites due to the technical difficulties in preparing samples suitable for nanomechanical testing. Liu *et al.* conducted real-time observation of the growth characteristics of sodium dendrites and simultaneous measurement of their mechanical properties using an environmental transmission electron microscope-atomic force microscope (ETEM-AFM) platform [215]. The measured maximum strength of the sodium dendrites reached up to 203 MPa, over 300 times higher than bulk Na. The results also show that the Na dendrites creep through the cracks and pores in SSEs, resulting in the failure of the battery. Therefore, reducing the defect size in the SSEs is crucial for mit-

igating battery failure induced by sodium dendrites. To sum up, the findings of this work provide important insights into mitigating dendritic short circuits in solid-state sodium metal batteries.

Furthermore, these characterization techniques also contribute to understanding cathode/electrolyte interface issues, such as interface kinetics and cathode/electrolyte reactions. Zhang's team used *in-situ* TEM to reveal the fundamental mechanism of Se catalytic conversion reactions in solid-state Na-SeS_2 nanobatteries [192]. The formation of amorphous Na-Se_xS_y, which significantly reduces the energy barrier of the redox reaction, was observed for the first time during the conversion process. Furthermore, the discoveries made by *in-situ* TEM guide the design of cathode components. Optimized composite cathodes in all-solid-state Na-SeS_2 batteries demonstrate excellent cycling capability based on the insights gained from *in-situ* TEM.

Before addressing interface issues, it is important to recognize that the bare Na metal's contact with ambient gases during production and transportation sets the initial conditions for SEI formation, thus establishing the initial conditions for subsequent anode and electrolyte interface reactions. Therefore, understanding the stability of metallic Na in dry air is crucial. Li *et al.* conducted a more in-depth study on the chemical reactions between alkali metals and ambient gases and improved the electrochemical performance of Na by controlling interface stability [216]. They used *in-situ* ETEM to observe the *in-situ* formation of Na metal particles in specifically designed solid-state cells under high vacuum. They found that to maintain the stability of Na in dry air, *in-situ* surface treatment (exposure to a CO_2 atmosphere) prior to the oxidation process, introducing a protective layer (Na_2CO_3), can address the issue of spontaneously forming low-quality oxide passivation layers.

Undoubtedly, the advanced characterization techniques and analysis methods mentioned above provide valuable insights into the structure, composition, and electrochemical properties of electrode/electrolyte interfaces. Nevertheless, it is essential to acknowledge that every technique or method possesses inherent limitations and disadvantages. Thus, it is imperative to employ a combination of multiple techniques to achieve comprehensive characterization and analysis, enabling us to derive dependable and precise conclusions. Bruce *et al.* from the University of Oxford employed T2 relaxation-diffusion magnetic resonance imaging (direct T2 contrast MRI) to investigate the interface microstructure of the Na/Na-β''-Al_2O_3/Na symmetric battery before and after cycling of the metallic Na electrode [217]. Additionally, to further visualize and validate the microstructure of the dendrites, Bruce combined other non-*in-situ* methods such as X-ray computed tomography and SEM to track and observe morphological changes inside the battery. Dendritic growth with a fractal morphology was observed in short-circuited cells, consistent with the ^{23}Na MRI results. The synergistic use of multiple methods mentioned above provides a deeper understanding of crack formation, microstructure growth, and the morphology of Na dendrites.

In summary, the intuitive and accurate clues obtained through various advanced characterization techniques provide insights for the development of new approaches to address electrode/electrolyte interface issues, thereby promoting research and development of high-performance all-solid-state SIBs. The continuous advancement and application of these techniques will further drive the progress of sodium battery technology, providing better solutions for sustainable energy storage.

7. Summary and outlook

All-solid-state SIBs are considered an ideal next-generation energy storage device for its significant cost and safety advantages. As the core part of all-solid-state SIBs, SSEs have captured the interest of researchers as they show great advantages in the cycling performance and safety performance of batteries. In this paper, we review the research progress of different types of inorganic SSEs, including the structure of electrolytes, synthesis methods, modification strategies, applications in SIBs and so on, as well as the surface design and advanced characterization of solid-state sodium battery interfaces.

Inorganic Na-ion SSEs have received a lot of attention due to their good electrochemical and safety properties, but there are some problems, such as alumina trioxide, the only commercially available Na-ion SSE, which has a low room temperature ionic conductivity. The modified Nasicon electrolyte has improved r.t. ionic conductivity and also has good chemical and electrochemical stability. However, there are interface problems with the electrodes. Sulfide electrolytes are soft in texture and have high r.t. ionic conductivity, but sulfides are poorly air-stable, *etc.* Based on these problems, scientists have made great efforts to improve the ionic conductivity and chemical/electrochemical stability of inorganic Na-ion SSEs.

In order to achieve practical applications of all-solid-state SIBs, we believe that future research will focus mainly on the following parts: (1) The role of Na-ion SSEs in cathode mixture of all-solid-state SIBs needs to be unraveled. Clarifying the relationship between redox activity and electrochemical stability in Na-ion SSEs is crucial. This aids in guiding the interface and material design for all-solid-state SIBs. (2) Na-ion halide electrolytes offer advantages over Na-ion sulfide electrolytes in terms of lower interfacial impedance and higher voltage stability. However, their application is currently limited by their lower ionic conductivity at room temperature. Significant progress has been made in developing novel electrolytes with high room temperature sodium ion conductivity, with an increasing number of sodium halide solid electrolytes exhibiting superior conductivity being reported. Therefore, the development of Na-ion halide electrolytes with excellent comprehensive performance can facilitate their application in the field of all-solid-state SIBs. (3) The thickness of the electrolyte is crucial for the energy density of the battery. Therefore, the design of electrolyte membranes based on current Na-ion SSEs is significant for the practical application of all-solid-state SIBs.

Thus, the development of all-solid-state SIBs still face various challenges that require further exploration and investigation.

Declaration of competing interest

The authors declare that they have no known competing financial interests or personal relationships that could have appeared to influence the work reported in this paper.

Acknowledgments

This work was supported by the National Natural Science Foundation of China (Nos. 22175070, 22293041). This work was also supported by the National Key Research and Development Program (Nos. 2021YFB2500200, 2021YFB2400300), the National Natural Science Foundation of China (No. 52177214), and China Fujian Energy Devices Science and Technology Innovation Laboratory Open Fund (No. 21C-OP202211).

References

[1] K. Song, C. Liu, L. Mi, et al., Small 17 (2021) e1903194.
[2] C. Yang, S. Xin, L. Mai, et al., Adv. Energy Mater. 11 (2020) 2000974.
[3] J. Hwang, S. Myung, Y. Sun, Chem. Soc. Rev. 46 (2017) 3529–3614.
[4] Z. Jiang, C. Yu, S. Chen, et al., Scripta Mater. 227 (2023) 115303.
[5] Z. Wang, C. Tang, Z. Wang, et al., Energy Mater. Adv. 4 (2023) 1–13.
[6] Q. Zhang, X. Shen, Q. Zhou, et al., Energy Mater. Adv. 2022 (2022) 1–11.
[7] L. Shen, S. Deng, R. Jiang, et al., Energy Storage Mater. 46 (2022) 175–181.
[8] H. Wan, J. Mwizerwa, F. Han, et al., Nano Energy 66 (2019) 104109.

[9] H. Wan, W. Weng, F. Han, et al., Nano Today 33 (2020) 100860.
[10] H. Wan, J. Mwizerwa, X. Qi, et al., ACS Appl. Mater. Interfaces 10 (2018) 12300–12304.
[11] Y. Yuno fano, J. Kummer, J. Inorg, Nuclear Chem. 29 (1967) 2453–2466.
[12] F. Colò, F. Bella, J.R. Nair, et al., J. Power Sources 365 (2017) 293–302.
[13] J. Wu, R. Zhang, Q. Fu, et al., Adv. Funct. Mater. 31 (2020) 2008165.
[14] G. Liu, X. Sun, X. Yu, et al., Chem. Engin. J. 420 (2021) 127692.
[15] R. Zhao, Y. Wu, Z. Liang, et al., Energy Environ. Sci. 13 (2020) 2386–2403.
[16] W. Richards, L. Miara, Y. Wang, et al., Chem. Mater. 28 (2015) 266–273.
[17] Z. Zhang, S. Wenzel, Y. Zhu, et al., ACS Appl. Energy Mater. 3 (2020) 7427–7437.
[18] L. Shen, J. Yang, G. Liu, et al., Mater. Today Energy 20 (2021) 100691.
[19] Y. Wang, S. Song, C. Xu, et al., Nano Mater. Sci. 1 (2019) 91–100.
[20] G. Huang, P. Zheng, W. Li, et al., Funct. Mater. Lett. 14 (2021) 2130005.
[21] X. Zhu, K. Wang, Y. Xu, et al., Energy Storage Mater. 36 (2021) 291–308.
[22] E. Quartarone, P. Mustarelli, Chem. Soc. Rev. 40 (2011) 2525–2540.
[23] L. Ran, A. Baktash, M. Li, et al., Energy Storage Mater. 40 (2021) 282–291.
[24] P. Ding, Z. Lin, X. Guo, et al., Mater. Today 51 (2021) 449–474.
[25] L. Gao, B. Tang, H. Jiang, et al., Adv. Sustain. Syst. 6 (2021) 2100389.
[26] A. Li, X. Liao, H. Zhang, et al., Adv. Mater. 32 (2020) e1905517.
[27] L. Tian, Y. Liu, Z. Su, et al., J. Mater. Chem. A 9 (2021) 23882–23890.
[28] L. Yue, J. Ma, J. Zhang, et al., Energy Storage Mater. 5 (2016) 139–164.
[29] Q. Zhao, P. Chen, S. Li, et al., J. Mater. Chem. A 7 (2019) 7823–7830.
[30] G. Wang, X. Zhu, A. Rashid, et al., J. Mater. Chem. A 8 (2020) 13351–13363.
[31] A. Manthiram, X. Yu, S. Wang, Nat. Rev. Mater. 2 (2017) 16103.
[32] J. Zhang, J. Zhao, L. Yue, et al., Adv. Energy Mater. 5 (2015) 1501082.
[33] H. Wang, Y. Chen, Z.D. Hood, et al., Angew. Chem. Int. Ed. 55 (2016) 8551–8555.
[34] S. He, Y. Xu, Y. Chen, et al., J.Mater. Chem. A 8 (2020) 12594–12602.
[35] S. Takeuchi, K. Suzuki, M. Hirayama, et al., J. Solid State Chem. 265 (2018) 353–358.
[36] Z. Wu, S. Chen, C. Yu, et al., Chem. Engin. J. 442 (2022) 136346.
[37] H. Hong, Mat. Res. Bull. 11 (1976) 173–182.
[38] J. Goodenough, H. Hong, A. Kafalas, Mat. Res. Bull. 11 (1976) 203–220.
[39] M. Evstigneeva, V. Nalbandyan, A. Petrenko, et al., Chem. Mater. 23 (2011) 1174–1181.
[40] W. Xia, Y. Zhao, F. Zhao, et al., Chem. Rev. 122 (2022) 3763–3819.
[41] Y. Sadikin, M. Brighi, P. Schouwink, et al., Adv. Energy Mater. 5 (2015) 1501016.
[42] Y. Qie, S. Wang, S. Fu, et al., J. Phys. Chem. Lett. 11 (2020) 3376–3383.
[43] X. He, Y. Zhu, Y. Mo, Nat. Commun. 8 (2017) 15893.
[44] G. Liu, J. Yang, J. Wu, et al., Adv. Mater. 36 (2024) 2311475.
[45] C. Delmas, Adv. Energy Mater. 8 (2018) 1703137.
[46] K. Hueso, M. Armand, T. Rojo, Energy Environ. Sci. 6 (2013) 734–749.
[47] H. Li, H. Fan, Z. Liu, et al., Sens. Actuator. B: Chem. 255 (2018) 1445–1454.
[48] X. Lu, G. Xia, J.P. Lemmon, et al., J. Power Sources 195 (2010) 2431–2442.
[49] S. Lee, D. Lee, S. Lee, et al., Bull. Mater. Sci. 39 (2016) 729–735.
[50] G. Yamaguchi, Bull. Chem. Soc. Jpn. 41 (1968) 93–99.
[51] M. Peters, J. Phys. Chem. 73 (1969) 1774–1780.
[52] L. Boyer, P. Edwardson, Ferroelectrics 104 (1990) 417–422.
[53] R. Niewa, Z. Anorg. Allg. Chem. 639 (2013) 1699–1715.
[54] S. Fan, M. Lei, H. Wu, et al., Energy Storage Mater. 31 (2020) 87–94.
[55] H. Nguyen, S. Hy, E. Wu, et al., J. Electrochem. Soc. 163 (2016) A2165–A2171.
[56] Y. Yu, Z. Wang, G. Shao, J. Mater. Chem. A 6 (2018) 19843–19852.
[57] C. Wei, R. Wang, Z. Wu, et al., Chem. Engin. J. 476 (2023) 146531.
[58] C. Wei, C. Yu, R. Wang, et al., J. Power Sources 559 (2023) 232659.
[59] C. Wei, S. Chen, C. Yu, et al., Appl. Mater. Today 31 (2023) 101770.
[60] C. Wei, C. Liu, Y. Xiao, et al., Adv. Funct. Mater. 34 (2024) 2314306.
[61] Q. Luo, C. Yu, C. Wei, et al., Ceram. Int. 49 (2023) 11485–11493.
[62] Z. Zhang, E. Ramos, F. Lalère, et al., Energy Environ. Sci. 11 (2018) 87–93.
[63] H. Oguchi, M. Matsuo, S. Kuromoto, et al., J. Appl. Phys. 111 (2012) 036102.
[64] M. Matsuo, S. Kuromoto, T. Sato, et al., Appl. Phys. Lett. 100 (2012) 203904.
[65] T. Udovic, M. Matsuo, A. Unemoto, et al., Chem. Commun. 50 (2014) 3750–3752.
[66] S. Shan, L. Yang, X. Liu, et al., J. Alloys Compd. 563 (2013) 176–179.
[67] S. Butee, K. Kambale, M. Firodiya, Process. Appl. Ceram. 10 (2016) 67–72.
[68] L. Ghadbeigi, A. Szendrei, P. Moreno, et al., Solid State Ionics 290 (2016) 77–82.
[69] S. Naqash, F. Tietz, E. Yazhenskikh, et al., Solid State Ionics 336 (2019) 57–66.
[70] Z. Zhang, S. Shi, Y. Hu, et al., J. Inorg. Mater. 28 (2013) 1255–1260.
[71] S. Yubuchi, A. Hayashi, M. Tatsumisago, Chem. Lett. 44 (2015) 884–886.
[72] T. Kim, K. Park, Y. Choi, et al., J. Mater. Chem. A 6 (2018) 840–844.
[73] A. Virkar, R. Gordon, J. Am. Ceram. Soc. 60 (1977) 58–61.
[74] C. Zhu, J. Xue, J. Alloys Compd. 517 (2012) 182–185.
[75] X. Wei, Y. Cao, L. Lu, et al., J. Alloys Compd. 509 (2011) 6222–6226.
[76] D. Xu, H. Jiang, Y. Li, et al., Eur. Phys. J. Appl. Phys. 74 (2016) 10901.
[77] L. Yang, S. Shan, X. Wei, et al., Ceram. Int. 40 (2014) 9055–9060.
[78] H. Erkalfa, Z. Baykara, Ceram. Int. 24 (1998) 81–90.
[79] G. Chen, J. Lu, X. Zhou, et al., Ceram. Int. 42 (2016) 16055–16062.
[80] C. Zhu, Y. Hong, P. Huang, J. Alloys Compd. 688 (2016) 746–751.
[81] Y. Viswanathan, A. Virkar, J. Mater. Sci. 18 (1983) 109–113.
[82] K. Yuria Saito, T. Asai, H. Kageyama, et al., Solid State Ionics 58 (1992) 327–331.
[83] A. Winand, P. Tarte, J. Mater. Sci. 25 (1990) 4008–4013.
[84] T. Miyajim, J. Tamaki, M. Matsuoka, et al., Solid State Ionics 124 (1999) 201–211.
[85] K. Koji Kawada, T. Okura, Funct. Mater. Lett. 14 (2021) 2141001.
[86] M. Guin, F. Tietz, J. Power Sources 273 (2015) 1056–1064.
[87] Q. Ma, M. Guin, S. Naqash, et al., Chem. Mater. 28 (2016) 4821–4828.
[88] M. Samiee, B. Radhakrishnan, Z. Rice, et al., J. Power Sources 347 (2017) 229–237.
[89] A. Jolley, G. Cohn, G. Hitz, et al., Ionics 21 (2015) 3031–3038.
[90] L. Liu, X. Qi, Y. Shao, et al., Energy Storage Sci. Techonol. 6 (2017) 961–980.
[91] S. He, Y. Xu, X. Ma, et al., ChemElectroChem 7 (2020) 2087–2094.
[92] S. Pal, R. Saha, G. Kumar, et al., J. Phys. Chem. C 124 (2020) 9161–9169.
[93] Y. Jing, G. Liu, M. Avdeev, et al., ACS Energy Lett. 5 (2020) 2835–2841.
[94] R. Fuentes, F. Figueiredo, M. Soares, et al., J. Eur. Ceram. Soc. 25 (2005) 455–462.
[95] A. Ignaszak, P. Pasierb, R. Gajerski, et al., Thermochim. Acta 426 (2005) 7–14.
[96] B. Yan, L. Kang, M. Kotobuki, et al., Mater. Technol. 34 (2018) 356–360.
[97] F. Ejehi, S. Marashi, M. Ghaani, et al., Ceram. Int. 38 (2012) 6857–6863.
[98] H. Leng, J. Huang, J. Nie, et al., J. Power Sources 391 (2018) 170–179.
[99] S. Liu, C. Zhou, Y. Wang, et al., ACS Appl. Mater. Interfaces 12 (2020) 3502–3509.
[100] J. Oh, L. He, A. Plewa, et al., ACS Appl. Mater. Interfaces 11 (2019) 40125–40133.
[101] Y. Shao, G. Zhong, Y. Lu, et al., Energy Storage Mater. 23 (2019) 514–521.
[102] Y. Li, Z. Deng, J. Peng, et al., Chem. Eur. J. 24 (2018) 1057–1061.
[103] J. Wu, Q. Wang, X. Guo, J. Power Sources 402 (2018) 513–518.
[104] Z. Deng, J. Gu, Y. Li, et al., Electrochim. Acta 298 (2019) 121–126.
[105] R. Smaha, J. Roudebush, J. Herb, et al., Inorg. Chem. 54 (2015) 7985–7991.
[106] Y. Wang, Q. Wang, Z. Liu, et al., J. Power Sources 293 (2015) 735–740.
[107] P. Hong Fang, ACS Appl. Mater. Interfaces 11 (2019) 963–972.
[108] Y. Sun, Y. Wang, X. Liang, et al., J. Am. Chem. Soc. 141 (2019) 5640–5644.
[109] H. Zhang. Lei Gao, Y. Wang, et al., J. Mater. Chem. A 8 (2020) 21265–21272.
[110] T. Wan, Z. Lu, Ciucci F, J. Power Sources 390 (2018) 61–70.
[111] M. Clarke. B. Goldmann, J. Dawson, et al., J. Mater. Chem. A 10 (2022) 2249–2255.
[112] C. Cazorla, D. Errandonea, Phys. Rev. Lett. 113 (2014) 235902.
[113] A. Barriocanal, M. Varela, Z. Sefrioui, et al., Science 321 (2008) 676–680.
[114] Y. Wang, T. Wen, C. Park, et al., J. Appl. Phys. 119 (2016) 025901.
[115] N. Tanibata, K. Noi, A. Hayashi, et al., ChemElectroChem 1 (2014) 1130–1132.
[116] A. Hayashi, N. Masuzawa, S. Yubuchi, et al., Nat. Commun. 10 (2019) 5266.
[117] A. Banerjee, K.H. Park, J.W. Heo, et al., Angew. Chem. Int. Ed. 55 (2016) 9634–9638.
[118] L. Zhang, D. Zhang, K. Yang, et al., Adv. Sci. 3 (2016) 1600089.
[119] Z. Yu, S.L. Shang, J.H. Seo, et al., Adv. Mater. 29 (2017) 1605561.
[120] W. Weng, G. Liu, Y. Li, et al., Appl. Mater. Today 27 (2022) 101448.
[121] L. Zhang, K. Yang, J. Mi, et al., Adv. Energy Mater. 5 (2015) 1501294.
[122] S. Bo, Y. Wang, J.C. Kim, et al., Chem. Mater. 28 (2015) 252–258.
[123] I. Chu, C. Kompella, H. Nguyen, et al., Sci. Rep. 6 (2016) 33733.
[124] C. Moon, H. Lee, K. Park, et al., ACS Energy Lett. 3 (2018) 2504–2512.
[125] M. Duchardt, S. Neuberger, U. Ruschewitz, et al., Chem. Mater. 30 (2018) 4134–4139.
[126] H. Jia, X. Liang, T. An, et al., Chem. Mater. 32 (2020) 4065–4071.
[127] S. Shang, Z. Yu, Y. Wang, et al., ACS Appl. Mater. Interfaces 9 (2017) 16261–16269.
[128] M. Meyer, Z. Anorg, Allg. Chem. 621 (1995) 457–463.
[129] T. Asano, A. Sakai, S. Ouchi, et al., Adv. Mater. 30 (2018) e1803075.
[130] S. Wang, Q. Bai, A.M. Nolan, et al., Angew. Chem. Int. Ed. 58 (2019) 8039–8043.
[131] M. Gombotz, H.M.R. Wilkening, ACS Sustain. Chem. Eng. 9 (2020) 743–755.
[132] R. Schlem, A. Banik, S. Ohno, et al., Chem. Mater. 33 (2021) 327–337.
[133] S. Chen, C. Yu, C. Wei, et al., Energy Mater. Adv. 4 (2023) 1–10.
[134] E. Wu, S. Banerjee, H. Tang, et al., Nat. Commun. 12 (2021) 1256.
[135] L. Li, J. Yao, R. Xu, et al., Energy Storage Mater. 63 (2023) 103016.
[136] X. Xu, Y. Li, X. Wang, et al., J. Solid State Electrochem. 28 (2024) 3501–3507.
[137] J. Fu, S. Wang, D. Wu, et al., Adv. Mater. 36 (2024) 2308012.
[138] Y. Hu, J. Fu, J. Xu, et al., Matter 7 (2024) 1018–1034.
[139] W. Tang, A. Unemoto, W. Zhou, et al., Energy Environ. Sci. 8 (2015) 3637–3645.
[140] L. Duchene, R.S. Kuhnel, D. Rentsch, et al., Chem. Commun. 53 (2017) 4195–4198.
[141] W. Tang, M. Matsuo, H. Wu, et al., Energy Storage Mater. 4 (2016) 79–83.
[142] X. Luo, A. Rawal, M.S. Salman, et al., ACS Appl. Nano Mater. 5 (2022) 373–379.
[143] J. Oh, L. He, B. Chua, et al., Energy Storage Mater. 34 (2021) 28–44.
[144] D. Reed, G. Coffey, E. Mast, et al., J. Power Sources 227 (2013) 94–100.
[145] I. Kim, J. Park, C. Kim, et al., J. Power Sources 301 (2016) 332–337.
[146] G. Zhang, Z. Wen, X. Wu, et al., J. Alloys Compd. 613 (2014) 80–86.
[147] C. Zhao, L. Liu, X. Qi, et al., Adv. Energy Mater. 8 (2018) 1703012.
[148] K. Zhao, Y. Liu, S. Zhang, et al., Electrochem. Commun. 69 (2016) 59–63.
[149] H. Yang, B. Zhang, K. Konstantinov, et al., Adv. Energy Sustain. Res. 2 (2021) 2000057.
[150] H. Lai, J. Wang, M. Cai, et al., Chem. Engin. J. 433 (2022) 133545.
[151] M. Bay, M. Wang, R. Grissa, et al., Adv. Energy Mater. 10 (2019) 1902899.
[152] L. Liu, X. Qi, Q. Ma, et al., ACS Appl. Mater. Interfaces 8 (2016) 32631–32636.
[153] P. Kehne, C. Guhl, L. Alff, et al., Solid State Ionics 341 (2019) 115041.
[154] C. Li, R. Li, K. Liu, et al., Interdisciplinary Mater. 1 (2022) 396–416.
[155] Z. Zhang, Q. Zhang, J. Shi, et al., Adv. Energy Mater. 7 (2017) 1601196.
[156] Y. Li, M. Li, Z. Sun, et al., Energy Storage Mater. 56 (2023) 582–599.
[157] H. Gao, L. Xue, S. Xin, et al., Angew. Chem. Int. Ed. 56 (2017) 5541–5545.
[158] W. Zhou, Y. Li, S. Xin, et al., ACS Cent. Sci. 3 (2017) 52–57.

[159] L. Ran, M. Li, E. Cooper, et al., Energy Storage Mater. 41 (2021) 8–13.
[160] X. Miao, H. Di, X. Ge, et al., Energy Storage Mater. 30 (2020) 170–178.
[161] X. Wang, J. Chen, Z. Mao, et al., J. Mater. Chem. A 9 (2021) 16039–16045.
[162] H. Fu, Q. Yin, Y. Huang, et al., ACS Mater. Lett. 2 (2019) 127–132.
[163] X. Yu, Y. Yao, X. Wang, et al., Energy Storage Mater. 54 (2023) 221–226.
[164] Q. Ni, Y. Xiong, Z. Sun, et al., Adv. Energy Mater. 13 (2023) 2300271.
[165] Y. Lu, J.A. Alonso, Q. Yi, et al., Adv. Energy Mater. 9 (2019) 1901205.
[166] C. Wang, Z. Sun, Y. Zhao, et al., Small 17 (2021) e2103819.
[167] Y. Zhao, C. Wang, Y. Dai, et al., Nano Energy 88 (2021) 106293.
[168] D. Li, C. Sun, C. Wang, et al., Energy Storage Mater. 54 (2023) 403–409.
[169] J. Yang, G. Liu, M. Avdeev, et al., ACS Energy Lett. 5 (2020) 2835–2841.
[170] Z. Jiang, S. Chen, C. Wei, et al., Chin. Chem. Lett. 35 (2024) 108561.
[171] J. Liang, X. Li, C. Wang, et al., Energy Mater. Adv. 4 (2023) 1–14.
[172] Q. Luo, L. Ming, D. Zhang, et al., Energy Mater. Adv. 4 (2023) 1–12.
[173] L. Ming, D. Liu, Q. Luo, et al., Chin. Chem. Lett. (2023) 109087.
[174] B. Tang, P. Jaschin, X. Li, et al., Mater. Today 41 (2020) 200–218.
[175] J. Yue, F. Han, X. Fan, et al., ACS Nano 11 (2017) 4885–4891.
[176] R. Rao, H. Chen, L. Wong, et al., J. Mater. Chem. A 5 (2017) 3377–3388.
[177] Z. Yu, S.L. Shang, J. Seo, et al., Adv. Mater. 29 (2017) 1605561.
[178] Q. Liu, X. Zhao, Q. Yang, et al., Adv. Mater. Technol. 8 (2023) 2200822.
[179] Z. Zhang, H. Cao, M. Yang, et al., J. Energy Chem. 48 (2020) 250–258.
[180] Y. Nagata, K. Nagao, M. Deguchi, et al., Chem. Mater. 30 (2018) 6998–7004.
[181] F. Hao, X. Chi, Y. Liang, et al., Joule 3 (2019) 1349–1359.
[182] H. Tang, Z. Deng, Z. Lin, et al., Chem. Mater. 30 (2017) 163–173.
[183] Y. Li, W. Arnold, S. Halacoglu, et al., Adv. Funct. Mater. (2021) 31.
[184] Y. Tian, Y. Sun, D.C. Hannah, et al., Joule 3 (2019) 1037–1050.
[185] Z. Wang, L. Zhang, X. Shang, et al., Chem. Eng. J. 428 (2022) 123094.
[186] L. Li, R. Xu, L. Zhang, et al., Adv. Funct. Mater. 32 (2022) 2203095.
[187] H. Wan, J.P. Mwizerwa, X. Qi, et al., ACS Nano 12 (2018) 2809–2817.
[188] H. Wan, J.P. Mwizerwa, X. Qi, et al., ACS Appl. Mater Interfaces 10 (2018) 12300–12304.
[189] J. Yue, X. Zhu, F. Han, et al., ACS Appl. Mater Interfaces 10 (2018) 39645–39650.
[190] X. Chi, Y. Liang, F. Hao, et al., Angew. Chem. Int. Ed. 57 (2018) 2630–2634.
[191] T. An, H. Jia, L. Peng, et al., ACS Appl. Mater. Interfaces 12 (2020) 20563–20569.
[192] Z. Zhang, Z. Wang, L. Zhang, et al., Adv. Sci. 9 (2022) e2200744.
[193] J. Park, J.P. Son, W. Ko, et al., ACS Energy Lett. 7 (2022) 3293–3301.
[194] X. Chi, Y. Zhang, F. Hao, et al., Nat. Commun. 13 (2022) 2854.
[195] M. Braga, N. Grundish, A. Murchison, et al., Energy Environ. Sci. 10 (2017) 331–336.
[196] R. Jiang, C. Song, J. Yang, et al., Adv. Funct. Mater. 33 (2023) 2301635.
[197] Y. Pang, Y. Liu, J. Yang, et al., Mater. Today Nano 18 (2022) 100194.
[198] L. de Kort, O. Brandt Corstius, V. Gulino, et al., Adv. Funct. Mater. 33 (2023) 2209122.
[199] J. Cuan, Y. Zhou, T. Zhou, et al., Adv. Mater. 31 (2019) e1803533.
[200] D. Souza, A. D'Angelo, T. Humphries, et al., Dalton Trans. 51 (2022) 13848–13857.
[201] W. Tang, K. Yoshida, A. Soloninin, et al., ACS Energy Lett. 1 (2016) 659–664.
[202] T.K. Yoshida, A. Unemoto, M. Matsuo, et al., Appl. Phys. Lett. 110 (2017) 103901.
[203] L. Duchêne, R. Kühnel, E. Stilp, et al., Energy Environ. Sci. 10 (2017) 2609–2615.
[204] L. Duchene, D.H. Kim, Y.B. Song, et al., Energy Storage Mater. 26 (2020) 543–549.
[205] F. Murgia, M. Brighi, R. Černý, Electrochem. Commun. 106 (2019) 106534.
[206] M. Brighi, F. Murgia, Z. Łodziana, et al., J. Power Sources 404 (2018) 7–12.
[207] L. He, H. Lin, H. Li, et al., J. Power Sources 396 (2018) 574–579.
[208] R. Asakura, D. Reber, L. Duchêne, et al., Energy Environ. Sci. 13 (2020) 5048–5058.
[209] M. Jin, S. Cheng, Z. Yang, et al., Chem. Engin. J. 455 (2023) 140904.
[210] L. Duchêne, D.H. Kim, Y.B. Song, et al., Energy Storage Mater. 26 (2020) 543–549.
[211] K. Niitani, S. Ushiroda, H. Kuwata, et al., ACS Energy Lett. 7 (2021) 145–149.
[212] J. Fu, S. Wang, D. Wu, et al., Adv. Mater. 36 (2024) e2308012.
[213] L. Geng, C. Zhao, J. Yan, et al., J. Mater. Chem. A 10 (2022) 14875–14883.
[214] L. Geng, D. Xue, J. Yao, et al., Energy Environ. Sci. 16 (2023) 2658–2668.
[215] Q. Liu, L. Zhang, H. Sun, et al., ACS Energy Lett. 5 (2020) 2546–2559.
[216] Y. Li, Q. Liu, S. Wu, et al., J. Am. Chem. Soc. 19 (2023) 10576–10583.
[217] G. Rees, D.Spencer Jolly, Z. Ning, et al., Angew. Chem. Int. Ed. 60 (2021) 2110–2115.